

Interplay of magnetic field and chemical potential induced anisotropy and frame dependent chaos of a $Q\bar{Q}$ pair in holographic QCD

Bhaskar Shukla,^{1,*} Jasper Nongmaithem,^{1,†} David Dudal,^{2,‡} and Subhash Mahapatra^{1,§}

¹*Department of Physics and Astronomy, National Institute of Technology Rourkela, Rourkela - 769008, India*

²*KU Leuven Campus Kortrijk – Kulak, Department of Physics,
Etienne Sabbelaan 53 bus 7657, 8500 Kortrijk, Belgium*

We investigate the role of both magnetic field and chemical potential on the emergence of chaotic dynamics in the QCD confining string from the holographic principle. An earlier developed bottom-up model of Einstein-Maxwell-dilaton gravity, which mimics QCD features quite well, is used. The qualitative information about the chaos is obtained using the Poincaré sections and Lyapunov exponents. Our results depend quite strongly on the frame we consider in the analysis. In the string frame, the chemical potential and the magnetic field suppress the chaotic dynamics in both parallel and perpendicular orientations of the string with respect to the magnetic field. Meanwhile, in the Einstein frame, the magnetic field suppresses/enhances the chaotic dynamics when the string is orientated perpendicular/parallel to the magnetic field, while the chemical potential enhances the chaotic dynamics for both orientations. We further analyse the MSS bound in the parameter space of the model and find it to be always satisfied in both frames.

I. INTRODUCTION

Whether quantum chromodynamics (QCD) exhibits chaotic behaviour at some level is a pivotal inquiry, holding significance for understanding QCD itself and the broader quest for a comprehensive understanding of interacting quantum field theories (QFT). Systems typically display chaotic characteristics in the natural world, except for some simple and isolated models. A parallel expectation is that QCD, a complex system, may inherently possess chaotic traits. Many researchers have worked on similar problems in recent years [1–8]. QCD is the fundamental QFT that underlies the precise understanding of subatomic particles such as quarks, gluons, and their interactions. Insights derived from weakly coupled approximations and out-of-time ordered correlators already indicate the possibility of chaos in QCD at high energies [9–12].

Notably, although lattice QCD is the most well-established approach for non-perturbative QCD studies, it does face limitations in capturing, e.g., time-dependent dynamics essential for analyzing chaos. Exploring alternative methodologies thus remains crucial in unraveling the delicate nature of chaos within the intricate realm of QCD. Since the introduction of the AdS/CFT correspondence [13–15], it has grown into a versatile way for exploring various aspects of strongly coupled quantum systems, also for analyzing strongly coupled and thus non-perturbative QCD.

The initial investigation on the chaotic dynamics of closed strings [16] sparked a series of subsequent studies examining the nature of chaos in the AdS/CFT [17–31]. In the holographic framework, we can utilize standard tools such as Poincaré sections and Lyapunov exponents to examine chaos [32–37]. Alternatively, not necessarily relying on holography and despite that the tools to quantitatively access quantum chaos are limited, there exist qualitative techniques like pole-skipping [38–40], out-of-time-order correlators (OTOC) [41–46], Krylov complexity [47–52] or random matrix theory (RMT) [53–58]. For a recent review on chaos in holography, see, for instance, [59].

Also, for classical chaos, the Lyapunov exponent characterizes the rate of separation of trajectories when subjected to initial condition perturbations [60]. A positive Lyapunov exponent indicates diverging trajectories, signifying a sensitive dependence on initial conditions, while a negative exponent suggests converging trajectories and a zero exponent signifies parallel trajectories. Notably, the Lyapunov exponent was also employed more recently to demonstrate the phase transition of AdS black holes [61–67]. A crucial insight was the establishment of an upper bound on the Lyapunov exponent known as the Maldacena-Shenker-Stanford (MSS) bound [68]. Mathematically,

$$\lambda \leq 2\pi T,$$

where T is the temperature of the system.

Another commonly employed technique for analyzing chaotic systems involves the utilization of the Poincaré section. This method entails tracing the trajectory of a dynamical variable within the system and selecting a specific section of that trajectory. The Poincaré section is characterized by a state space that is one dimension less than the original dynamical system. In essence,

* 519ph1003@nitrkl.ac.in

† 524ph6005@nitrkl.ac.in

‡ david.dudal@kuleuven.be

§ mahapatrasub@nitrkl.ac.in

this approach allows for a simplified representation that captures essential features of the system's behaviour while reducing the complexity associated with the complete system.

The holographic duality introduces a unique perspective, allowing for the exploration of quantum dynamical aspects in a dual, higher dimensional gravity (classical) system. In holography, classical strings are examined in higher dimensions, specifically in five dimensions, in the context of bottom-up or top-down holographic QCD models. Detailed analyses of chaos in the quark-antiquark pair have been performed within the AdS/CFT context already in e.g. [69–72].

Many external factors greatly influence QCD properties, particularly the chemical potential, magnetic field, and temperature. They are believed to be produced in central and/or non-central heavy ion collisions and are expected to be of the order of a hundred MeV [73–78]. The dynamical and equilibrium properties of QCD are expected to change considerably depending upon the magnitudes of such factors. It is well known that various intricate phases in QCD appear in the parameter space of chemical potential, magnetic field, and temperature. However, due to various analytical and numerical issues, a complete understanding of QCD in the parameter space of such factors is still far from fully understood. For instance, studying the impact of chemical potential in lattice QCD poses challenges owing to the sign problem. The intricacies associated with this issue make it difficult to explore the effects comprehensively. As mentioned above, the situation worsens when one tries to address dynamic problems.

Much work has been done in recent years to study QCD-like physics from holography. By now various top-down and bottom-up holographic models have been constructed whose dual boundary field theories try to mimic real QCD as closely as possible in all the parameter space of temperature, chemical potential, and magnetic field. This includes simple holographic models having temperature as the only relevant parameter [79–81], models with both temperature and chemical potential [82–85] or temperature and magnetic field [86–90], and models having all three parameters [91–94]. Using these holographic models, a lot of new insights into the characteristic structure of QCD at strong coupling have been obtained, and in some cases, new and interesting predictions have also been made. More discussion on holographic QCD in the presence of magnetic field and chemical potential can be found in [95–117], see also [118–120] for reviews of this exciting subject. Since holography provides a unique mathematical tool to investigate QCD at strong couplings, therefore it would be interesting to analyse whether this duality can also provide new insights into the chaotic structure of quark-antiquark pair, corresponding to the dynamics of the Wilson loop or the open string, when all interesting parameters such as the temperature, chemical potential, and magnetic field are simultaneously present in QCD background. In this work, we undertake such an analysis.

In this work, we use a recently proposed dynamical holographic QCD model [91], which includes both the magnetic field and the chemical potential to dynamically investigate and find anisotropic imprints of chaotic behaviour in the quark-antiquark pair. This particular model is not only analytically tractable but was also shown to be successful in capturing a variety of real QCD results from holography, including the inverse magnetisation phenomena, linear Regge trajectories for heavy vector mesons, area law for the Wilson loop, etc.

Another crucial observation in gravity research in general is that sometimes significant differences can arise between the string and Einstein frames' physics. Yet, the debate over which choice complies with the correct physical processes is still ongoing [121–130]. Specializing to our holographic case, in [32], it was observed that the magnetic field-dependent Poincaré sections and Lyapunov exponents of the perturbed string dynamics get substantially modified in different frames. In particular, the anisotropic features and magnitudes of chaotic observables changed considerably. Therefore, in this paper, we shall further investigate, in both frames, the chaotic nature of an open string using the QCD-gravity dual mentioned above, which includes both the magnetic field and the chemical potential. For simplicity, we work in the usual units $G = \hbar = c = k_B = 1$.

The paper is structured into five sections. In section II, we discuss the methodology, focusing on the bottom-up magnetised EMD gravity model, setting the stage with the necessary theoretical background. In section III, we examine the dynamics in the string frame, starting with the derivation of the string equation of motion in section III A, followed by the introduction of perturbations in section III B. This section also includes the Poincaré section analysis to visualise chaotic trajectories, section III C and the Lyapunov exponent analysis to quantify chaos, section III D. To complete our study, we also include the analysis of saddle points in section III E. In section IV, we repeat a similar calculation of the string dynamics within the Einstein frame. This includes Poincaré analysis in section IV B, Lyapunov exponents in section IV C, and MSS bound analysis in section IV D. Finally, in section V, we conclude our paper by highlighting the main results with some discussion.

II. MAGNETISED EMD GRAVITY WITH CHEMICAL POTENTIAL

In this section, we briefly discuss the holographic QCD model of [86, 91]. This will set the stage for later sections for investigating chemical potential and magnetic field effects on chaotic string dynamics. We start with a five-dimensional gravity system,

$$S = -\frac{1}{16\pi G_5} \int d^5x \sqrt{-g} \left[R - \frac{1}{4} f_1(\phi) F_{(1)MN} F^{MN} - \frac{1}{4} f_2(\phi) F_{(2)MN} F^{MN} - \frac{1}{2} \partial_M \phi \partial^M \phi - V(\phi) \right], \quad (1)$$

where $F_{(1)MN}$ and $F_{(2)MN}$ are two $U(1)$ field strength tensors used to introduce a background chemical potential (μ) and magnetic field (B) respectively, ϕ is the dilaton field, $f_1(\phi)$ and $f_2(\phi)$ are the coupling functions between the dilaton field and the two $U(1)$

gauge fields, $V(\phi)$ is the dilaton potential, and G_5 is Newton's gravitational constant in five dimensions.

By varying the action (1), we get the Einstein, gauge fields, and dilaton equations of motion. To determine solutions of these equations of motion, we take the following Ansätze

$$ds^2 = \frac{L_{AdS}^2 e^{2A(z)}}{z^2} \left[-g(z) dt^2 + \frac{dz^2}{g(z)} + dx_1^2 + e^{B^2 z^2} (dx_2^2 + dx_3^2) \right],$$

$$\phi = \phi(z), \quad A_{(1)M} = A_t(z) \delta_M^t, \quad F_{(2)MN} = B dx_2 \wedge dx_3, \quad (2)$$

where z is the usual holographic radial coordinate, $z = 1/r$, and L_{AdS} is the AdS length scale which we will set to "1" from now on. The above Ansätze gives us four Einstein, one gauge field (coming from the first gauge field $A_{(1)M}$), and one dilaton equation of motion. The gauge field equation of motion coming from the second gauge field $A_{(2)M}$ is trivially satisfied. Therefore, overall, there are six equations of motion. However, only five of them are independent. Interestingly, taking the dilaton equation as a constraint equation and using the potential reconstruction technique [83, 131–138], complete closed-form solutions to the gravity equations can be found. One particular solution corresponding to a black hole is given by

$$A(z) = -az^2, \quad (3)$$

$$f_1(z) = e^{-A(z) - B^2 z^2 - cz^2}, \quad (4)$$

$$g(z) = 1 + \frac{c \left(e^{z^2(3a-B^2+c)} (z^2(3a-B^2+c) - 1) + 1 \right) \mu^2}{\left(e^{cz_h^2} - 1 \right)^2 (3a-B^2+c)^2}$$

$$- \frac{\left(e^{z^2(3a-B^2)} (z^2(3a-B^2) - 1) + 1 \right) \left(\frac{c \left(e^{z_h^2(3a-B^2+c)} (z_h^2(3a-B^2+c) - 1) + 1 \right) \mu^2}{L^2 \left(e^{cz_h^2} - 1 \right)^2 (3a-B^2+c)^2} + 1 \right)}{e^{z_h^2(3a-B^2)} (z_h^2(3a-B^2) - 1) + 1}, \quad (5)$$

$$\phi(z) = \frac{(9a-B^2) \log \left(\sqrt{6a^2 - B^4} \sqrt{z^2(6a^2 - B^4) + 9a - B^2} + 6a^2 z - B^4 z \right)}{\sqrt{6a^2 - B^4}}$$

$$+ z \sqrt{z^2(6a^2 - B^4) + 9a - B^2} - \frac{(9a-B^2) \log \left(\sqrt{9a - B^2} \sqrt{6a^2 - B^4} \right)}{\sqrt{6a^2 - B^4}}, \quad (6)$$

$$f_2(z) = g(z) e^{2A(z) + 2B^2 z^2} \left(-\frac{6A'(z)}{z} - 4B^2 + \frac{4}{z^2} \right) - \frac{2e^{2A(z) + 2B^2 z^2} g'(z)}{z}, \quad (7)$$

$$V(z) = \frac{1}{2} e^{-2A(z)} (z (g'(z) (9 - 9zA'(z) - 4B^2 z^2) - zg''(z))$$

$$- 2g(z) (3z (zA''(z) + 3A'(z) (zA'(z) + B^2 z^2 - 2)) + 2(B^4 z^4 - 4B^2 z^2 + 6))). \quad (8)$$

This solution is obtained by imposing the boundary conditions

$$g(0) = 1, \quad g(z_h) = 0,$$

$$A_t(0) = \mu, \quad A_t(z_h) = 0,$$

$$A(0) = 0, \quad (9)$$

where z_h is the radius of the black hole horizon. Hence, the z -coordinate runs from $z = 0$ to $z = z_h$ (or $r = r_h$ to $r = \infty$), where $z = 0$ (or $r = \infty$) is the asymptotic boundary. These boundary conditions are chosen to ensure that the spacetime asymptotes to AdS at the asymptotic boundary $z \rightarrow 0$ and that it has a well-defined horizon at $z = z_h$. Apart from these boundary conditions, we have further demanded that the dilaton field ϕ remains real throughout the bulk and goes to zero at the asymptotic boundary $\phi(0) = 0$. Notice the presence of the magnetic field in the Ansätze metric, see Eq. (2), partially breaks the boundary $SO(3)$ symmetry, but recovers it as soon as $B \rightarrow 0$. Note that B is the 5-dimensional one, so it carries dimension of GeV.

The above solution explicitly depends on μ and B , with a and c being the only arbitrary and free parameters. The value of a and c is usually fixed by taking inputs from the dual boundary QCD theory. In [91, 139], $a = 0.15 \text{ GeV}^2$ was fixed by demanding the confinement/deconfinement transition temperature to be around 270 MeV at zero chemical potential and magnetic field. Similarly, the magnitude of c was determined by aligning the holographic meson mass spectrum with that of the lowest-lying heavy meson states. This fixes $c = 1.16 \text{ GeV}^2$. Moreover, for the dilaton field to be real, we must impose $B^4 \leq 6a^2$, further

putting a constraint on the maximally allowed magnetic field at $B \simeq 0.6$ GeV [86]. We want to emphasize that we are not considering varying magnetic field scenarios. We will consider it a constant throughout spacetime.

There are some features of this particular form of $A(z)$ that we have chosen in Eq. (3). As said, our metric is now asymptotically AdS, i.e., at $z \rightarrow 0$. This can also be checked from our potential form $V(z)$ in Eq. (8). As $z \rightarrow 0$, $V(z)$ reduces to the value of the cosmological constant expected in five-dimensional AdS spacetime. The form of our scalar potential satisfies the Gubser criterion [140], as it is bounded from above. Moreover, the mass of the scalar field also satisfies the Breitenlohner-Freedman bound [141]. Another solution to the gravity system also exists, one corresponding to thermal-AdS, which has no horizon. It can be obtained from the black hole solution by taking the limit $z_h \rightarrow \infty$. The black hole and thermal-AdS solutions correspond to the deconfined and confined phases of the dual boundary QCD, respectively, and can undergo magnetic field and chemical potential dependent Hawking/Page type phase transitions [106].

Since the chaotic nature of the string is intimately tied to the presence of the horizon, the thermal-AdS solution will not play any part in the rest of the discussion, and we will concentrate mainly on the black hole solution.

The metric function that we have solved is in the Einstein frame. In our previous analysis [32], it was observed that different frames had a significant impact on the chaotic nature of the string. In particular, the string frame metric takes a different form than the Einstein frame metric in the presence of a non-trivial dilaton field, thereby leading to different profiles of the Poincaré section and Lyapunov exponent in these two frames. We can thus expect to find further significant differences in the chaotic dynamics of the string when the chemical potential is also turned on.

Now, let us note the metric expression in the string frame. The standard way to go from the Einstein to the string frame metric involves the transformation $(g_s)_{MN} = e^{\sqrt{2/3}\phi} g_{MN}$ [91], where the subscript ‘‘s’’ stands for string frame. The metric solution (5) in the string frame then reads

$$ds^2 = L_{AdS}^2 r^2 e^{2A_s(r)} \left[-g(r) dt^2 + \frac{dr^2}{r^4 g(r)} + dx_1^2 + e^{\frac{B^2}{r^2}} (dx_2^2 + dx_3^2) \right], \quad (10)$$

where $A_s(r) = A(r) + \sqrt{1/6}\phi(r)$. Writing down the above Einstein and string frame metrics in the following general form

$$ds^2 = g_{tt} dt^2 + g_{11} dx_1^2 + g_{22} dx_2^2 + g_{33} dx_3^2 + g_{rr} dr^2, \quad (11)$$

will further allow us to write various expressions related to the string dynamics in a unified manner and we can minimise repetition of various expressions. Note that in the string frame, we have:

$$g_{tt} = -r^2 e^{2A_s(r)} g(r), \quad g_{11} = r^2 e^{2A_s(r)} h(r), \quad g_{22} = g_{33} = r^2 e^{2A_s(r)} q(r), \quad g_{rr} = \frac{e^{2A_s(r)}}{r^2 g(r)}, \quad (12)$$

with

$$h(r) = 1, \quad q(r) = e^{\frac{B^2}{r^2}}, \quad (13)$$

with similar expressions existing in the Einstein frame. With this complete picture of our five-dimensional metric, we can now move on to model our string system on it. In the next section, we will investigate the string dynamics in the string frame.

III. CHAOTIC DYNAMICS IN THE STRING FRAME

A. String model

In this section, we investigate the string dynamics and its chaotic behaviour in the presence of chemical potential and magnetic field at finite temperature. We use an infinitely thin string that traces out a world sheet as it moves through time. Its motion is determined by the Nambu-Goto action

$$S = -\frac{1}{2\pi\alpha'} \int \sqrt{-h} dl dt, \quad (14)$$

where α' is the string tension, h is the determinant of the induced metric $h_{\alpha\beta}$ on the world sheet

$$h_{\alpha\beta} = g_{(s)MN} \frac{\partial X^M}{\partial \xi^\alpha} \frac{\partial X^N}{\partial \xi^\beta}. \quad (15)$$

Here $g_{(s)}$ is the metric tensor in the string frame, and ξ^i are the coordinates on the string world sheet, i.e., $i = (t, \ell)$.

Let us first investigate the static string configuration. In the presence of a background magnetic field, we will consider two special cases of string configuration, either parallel or perpendicular to the magnetic field. Accordingly, there are two ways to parametrize the string. In the static case, the location of the string is specified by $r(\ell)$ and $x_i(\ell)$, with $i = 1$ when the magnetic field B is parallel to the string endpoints and $i = 3$ when perpendicular. Here, ℓ corresponds to a proper length measured along the string with endpoints of the string located at $x_i = \pm L/2$.

Following the above notation, the Nambu-Goto action of the static string looks

$$S = -\frac{1}{2\pi\alpha'} \int dt d\ell \sqrt{|g_{rr}g_{tt}(r')^2 + g_{ii}g_{tt}(x'_i)^2|}, \quad (16)$$

where the prime $'$ denotes the derivative with respect to ℓ . Notice that in the above Lagrangian, the coordinate x_i is cyclic. This gives us a conserved quantity

$$\frac{\partial \mathcal{L}}{\partial x'_i} = -\frac{1}{2\pi\alpha'} \frac{|g_{tt}|g_{ii}x'_i}{\sqrt{|g_{tt}|g_{ii}(x'_i)^2 + |g_{tt}|g_{rr}(r')^2}}. \quad (17)$$

At the tip of the string $r(\ell = 0) = r_0$, we have $\left. \frac{dr}{dx_i} \right|_{\ell=0} = 0$. This gives

$$\frac{g_{ii}\sqrt{|g_{tt}|}x'_i}{\sqrt{g_{rr}(r')^2 + g_{ii}(x'_i)^2}} = \sqrt{g_{ii}|g_{tt}|} \Big|_{\ell=0}. \quad (18)$$

The symmetry of the string configuration ensures that the tip r_0 lies at the point $x_i = 0$ (or $\ell = 0$). Using the elementary length element set by

$$d\ell^2 = g_{rr}dr^2 + g_{ii}dx_i^2, \quad (19)$$

we get the following static profile of the string

$$x' = \pm \frac{\sqrt{-g_{ii}(r_0)g_{tt}(r_0)}}{g_{ii}\sqrt{-g_{tt}}}, \quad (20)$$

$$r' = \pm \frac{\sqrt{g_{ii}(r_0)g_{tt}(r_0) - g_{ii}g_{tt}}}{\sqrt{-g_{tt}g_{rr}g_{ii}}}. \quad (21)$$

Using the boundary condition that the endpoints of the string lie on the asymptotic boundary at $x_i = \pm L/2$, we can further determine the string length L as a function of r_0

$$L = \int_{r_0}^{\infty} 2\sqrt{\frac{g_{rr}(r)}{g_{ii}(r)} \left(\frac{g_{ii}(r_0)g_{tt}(r_0)}{g_{ii}(r)g_{tt}(r) - g_{ii}(r_0)g_{tt}(r_0)} \right)} dr. \quad (22)$$

In Fig. 1, the behaviour of the string length L as a function of r_0 for different values of the chemical potential at a fixed magnetic field $B = 0.2$ aligned both in the parallel and perpendicular direction is shown. Here, we have taken $r_h = 1$ for illustration, but analogous results appear for other r_h values as well. There appears a maximal string length L_{max} , beyond which no connected solution exists, i.e., no solution to Eq. (22) exists for $L > L_{max}$. This behaviour is true irrespective of the values of μ and B . The precise value of this L_{max} , however, depends non-trivially on μ and B . In particular, it decreases with μ and B in parallel and perpendicular orientations. Moreover, below L_{max} , we can identify two types of connecting string solutions for each value of L , one where the tip of the string is near the black hole horizon (represented by dashed lines) and one where the tip of the string is away from the horizon (represented by dotted and solid lines).

We further need to probe their free energy profile to describe the stability of the connected string solutions. This can be computed from the on-shell Nambu-Goto action. For the string solutions in Eq. (22), the free energy is given by

$$F = -\frac{2}{2\pi\alpha'} \int_{r_0}^{\infty} \frac{\sqrt{-g_{tt}(r)g_{rr}(r)}}{\sqrt{\frac{g_{ii}(r_0)g_{tt}(r_0)}{g_{ii}(r)g_{tt}(r)} \left(\frac{g_{ii}(r)g_{tt}(r)}{g_{ii}(r_0)g_{tt}(r_0)} - 1 \right)}} dr. \quad (23)$$

Observe that in the limit $r \rightarrow \infty$, F contains a UV divergence. Generally, this can be taken care of by subtracting the free energy of the two disconnected strings that are separated by a distance L and extended from the boundary to the horizon. Since the disconnected strings are also solutions of the string equations of motion (EOMs), one may consider these disconnected

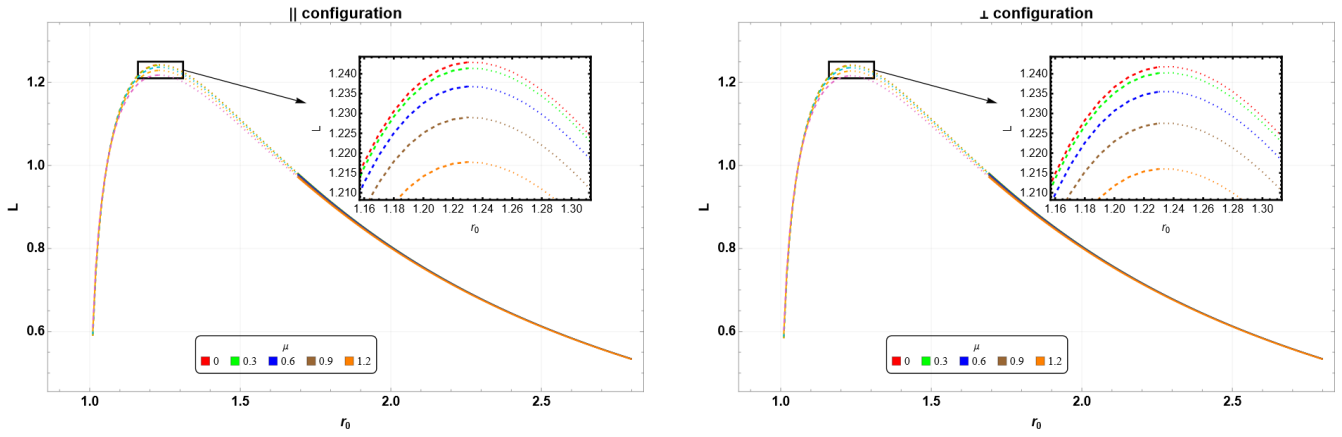


FIG. 1. The behaviour of the string length L as a function of r_0 is depicted for both parallel (left) and perpendicular (right) orientations of the string, in relation to the varying chemical potential μ , with the magnetic field fixed at $B = 0.2$ and horizon radius $r_h = 1$. All quantities are in units of GeV.

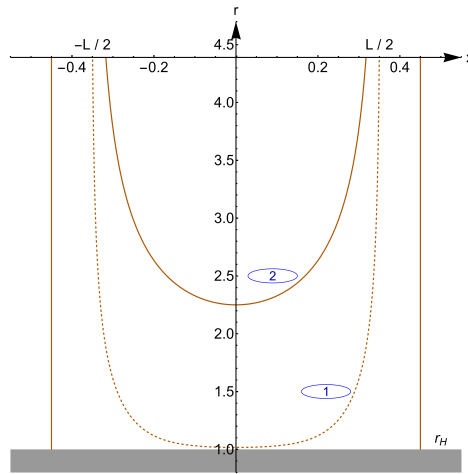


FIG. 2. The figure illustrates three distinct configurations of static suspended strings. The solid (2) and dashed (1) lines represent connected strings, corresponding to the local minima and maxima of the energy, respectively. The two solid, straight, parallel lines denote disconnected strings extending from the asymptotic boundary to the horizon. The parameters used are $B = 0.1$, $\mu = 0.2$, $r_h = 1$, and $L = 0.7$ for the parallel magnetic field. All quantities are expressed in units of GeV.

strings as the third string solution. Accordingly, there exist three string profiles (two connected and one disconnected) for $L < L_{max}$, whereas only the disconnected profile appears for $L > L_{max}$. These different string profiles are shown in Fig. 2, where two connected profiles are indicated by the solid line (corresponding to large r_0 solution), marked as (2) and the dashed line (corresponding to small r_0 solution) marked as (1). In contrast, two parallel solid vertical lines indicate the disconnected profile. The free energy of the disconnected string profile is given by

$$F_{dis} = -\frac{2}{2\pi\alpha'} \int_r^\infty \sqrt{-g_{tt}(r)g_{rr}(r)} dr. \quad (24)$$

Since the UV divergence structure of F and F_{dis} is the same, it allows us to regularise F in a minimalistic way.

The free energy behaviour is illustrated in Fig. 3, where the difference $\Delta F = F - F_{dis}$ is plotted. The dashed and solid lines again correspond to the small and large r_0 solutions, respectively. Analysing the free energy behaviour reveals a clear distinction between the large r_0 and small r_0 solutions. For the large r_0 configuration, it is consistently observed that this solution exhibits lower free energy compared to the small r_0 solution. This behaviour indicates that the true minimum energy state, and thus the most stable configuration, is associated with the large r_0 solution. Interestingly, the free energy of the large r_0 solution can exchange dominance relative to F_{dis} depending on the length L of the string. Specifically, there is a critical length L_{crit} at which $\Delta F = 0$, and the free energy is minimised by the large r_0 solution only for $L \leq L_{crit}$. This string configuration gives the stable phase of the string configuration for small L . Beyond this critical length, for $L_{crit} \leq L \leq L_{max}$, the reference-free

energy F_{dis} becomes minimum, indicating a metastable phase of the string configuration. Dotted lines in Figs. 1 and 3 represent this metastable phase. On the other hand, the small r_0 solution consistently has free energy greater than F_{dis} , suggesting a higher and less stable energy state. The local maxima of the energy profile for the small r_0 solution is notably close to the horizon, emphasising its instability relative to the large r_0 and parallel string configurations. This unstable phase of the string configuration is represented by dashed lines in Figs. 1 and 3. This behaviour of the string's free energy is typical for both parallel and perpendicular magnetic field configurations for all possible chemical potential values.

To explore the chaotic dynamics of the string, we focus on the small r_0 solution, where the free energy is comparatively large. The small r_0 solution consistently exhibits higher free energy than the large r_0 solution, indicating a less stable and more energetically excited state - as we have observed earlier from its free energy. Additionally, one could expect that black holes, being thermal objects, might enhance or induce chaotic dynamics of the string as its tip approaches the horizon.

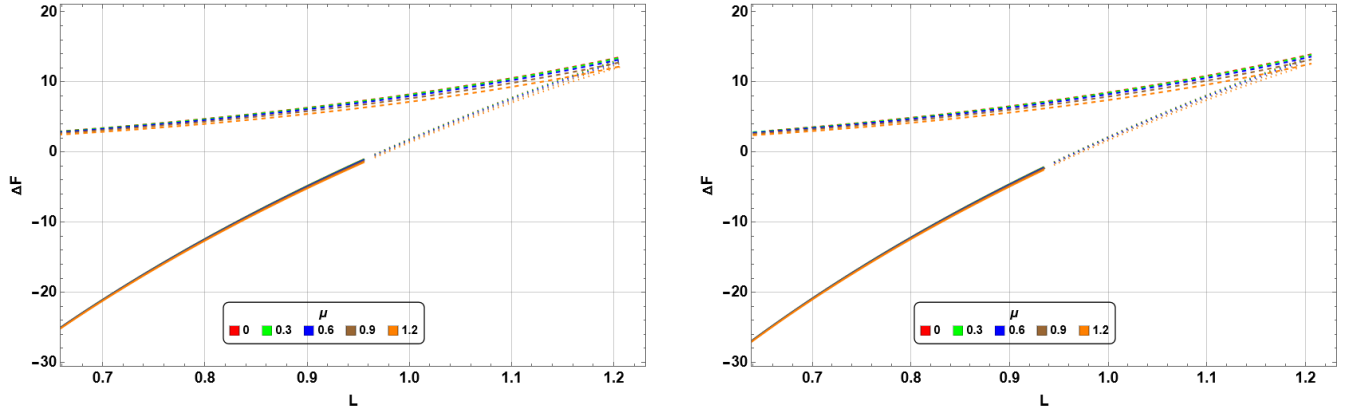


FIG. 3. The free energy difference is presented for the string in the x_1 (\parallel) configuration on the left and the x_3 (\perp) configuration on the right, at a magnetic field strength of 0.2 GeV, across different values of the chemical potential μ .

B. Perturbing the string

Probing chaotic dynamics of any system requires that we introduce slight perturbations to the initial condition of the system, giving us information on how the dynamics change w.r.t. the other initial conditions. In particular, we consider a time-dependent perturbation around the static string solution and expand the Nambu-Goto action order by order in this perturbation.

To begin such analysis, we choose a specific value of the string length L that lies in the unstable area. As we have seen from the previous demonstration of the free energy diagram (Fig. 3) and the length solution diagram (Fig. 1), the unstable area corresponds to the small r_0 case, i.e., r_0 near the black hole horizon. Introducing the perturbation as

$$r(t, \ell) = n^r(\ell)\xi(t, \ell) + r_b(\ell), \quad (25)$$

and

$$x(t, \ell) = n^x(\ell)\xi(t, \ell) + x_b(\ell), \quad (26)$$

where $r_b(\ell)$ and $x_b(\ell)$ correspond to the static position, $\xi(t, \ell)$ is the small perturbation that carries our desired time-dependent part, and x is either x_1 (parallel) or x_3 (perpendicular) depending upon the orientation of the string with respect to the magnetic field. The normal vector $n^M = (0, n^x, 0, 0, n^r)$ is orthogonal to tangent vector t^M and makes sure the perturbation is perpendicular to the string profile. Accordingly,

$$\begin{aligned} (n^x)^2 g_{xx}(r) + (n^r)^2 g_{rr}(r) &= 1, \\ n^x g_{xx}(r)x'(\ell) + n^r g_{rr}(r)r'(\ell) &= 0. \end{aligned} \quad (27)$$

Next, we solve for the normal vectors n_x and n_r using the above equations. For an outward perturbation, as in Fig. 4, these are given by

$$n^x(\ell) = \sqrt{\frac{g_{rr}}{g_{xx}}} r'(\ell), \quad (28)$$

$$n^r(\ell) = -\sqrt{\frac{g_{xx}}{g_{rr}}} x'(\ell). \quad (29)$$

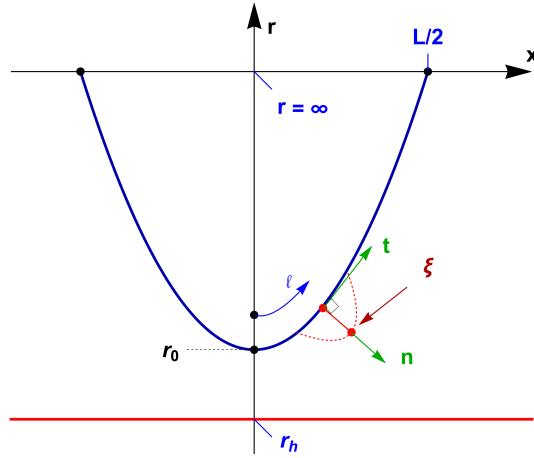


FIG. 4. An illustration of the static string profile and its normal perturbation.

With Eqs. (25) and (26), we can expand our action around the static configuration r_b and x_b up to any order in the perturbation parameter. For our analysis, we will be taking only up to the next-to-leading order term. The leading order generates an oscillatory term and the next-to-leading order produces a trapping potential. The expanded action contains quadratic order and cubic order terms in ξ . The quadratic part of the action has the form

$$S^{(2)} = \frac{1}{2\pi\alpha'} \int dt \int_{-\infty}^{\infty} d\ell \left(C_{\ell\ell}^{x_i} (\xi')^2 + C_{00}^{x_i} \xi^2 + \xi^2 C_{ii}^{x_i} \right), \quad (30)$$

where the prime ($'$) denotes a derivative w.r.t. ℓ and the dot (\cdot) w.r.t. t . The form of the coefficients C_{ii} , $C_{\ell\ell}$, and C_{00} are as follows

$$\begin{aligned} C_{ii}^{x_i} &= \frac{e^{-A_s(r_b(\ell))}}{2r_b(\ell)\sqrt{g(r_b(\ell))}}, \\ C_{\ell\ell}^{x_i} &= -\frac{1}{2}r_b(\ell)\sqrt{g(r_b(\ell))}e^{A_s(r_b(\ell))}, \\ C_{00}^{x_1} &= \frac{e^{-5A_s(r_b(\ell))}}{8r_b(\ell)^3g(r_b(\ell))^{3/2}h(r_b(\ell))^2} \\ &\quad (r_0^4g(r_0)h(r_0)e^{4A_s(r_0)}(r_b(\ell)g(r_b(\ell))(2h(r_b(\ell))(g'(r_b(\ell))(3r_b(\ell)A'_s(r_b(\ell))+1) - \\ &\quad r_b(\ell)g''(r_b(\ell)) + r_b(\ell)g'(r_b(\ell))h'(r_b(\ell))) + \\ &\quad 2g(r_b(\ell))^2(r_b(\ell)h'(r_b(\ell))(r_b(\ell)A'_s(r_b(\ell))+1) + \\ &\quad h(r_b(\ell))(r_b(\ell)^2(6A'_s(r_b(\ell))^2 - 2A''_s(r_b(\ell))) + 8r_b(\ell)A'_s(r_b(\ell))+4)) + \\ &\quad 2r_b(\ell)^2h(r_b(\ell))g'(r_b(\ell))^2 - r_b(\ell)^4g(r_b(\ell))^2e^{4A_s(r_b(\ell))}(2r_b(\ell)h(r_b(\ell))g'(r_b(\ell)) \\ &\quad (2h(r_b(\ell))(r_b(\ell)A'_s(r_b(\ell))+1) + r_b(\ell)h'(r_b(\ell))) + g(r_b(\ell))(2r_b(\ell) \\ &\quad h(r_b(\ell))(2h'(r_b(\ell))(r_b(\ell)A'_s(r_b(\ell))+2) + r_b(\ell) \\ &\quad h''(r_b(\ell))) + 4h(r_b(\ell))^2(r_b(\ell)^2(A'_s(r_b(\ell))^2 + A''_s(r_b(\ell))) + 4r_b(\ell)A'_s(r_b(\ell))+2) - \\ &\quad r_b(\ell)^2h(r_b(\ell))^2))), \end{aligned} \quad (31)$$

where $i = 1$ and $i = 3$ again correspond to the parallel and perpendicular magnetic field orientations, respectively. The expression of $C_{00}^{x_3}$ is identical to $C_{00}^{x_1}$, except $h(r)$ is to be replaced by $q(r)$. We determine the equation of motion from the perturbed action to analyse the dynamics. The equation of motion is given by

$$C_{ii}^{x_i} \ddot{\xi} + \partial_\ell (C_{\ell\ell}^{x_i} \xi') - C_{00}^{x_i} \xi = 0, \quad (32)$$

using the factorization $\xi(t, \ell) = \xi(\ell)e^{i\omega t}$, the above equation can be re-written into a Sturm-Liouville form

$$\partial_\ell (C_{\ell\ell}^{x_i} \xi') - C_{00}^{x_i} \xi = \omega^2 \xi C_{ii}^{x_i}, \quad (33)$$

where $W(\ell) = -C_{ii}^{x_i}(\ell)$ is the weight function, with inner product

$$(\xi, \zeta) \equiv \int_{-\infty}^{\infty} W(\ell) \xi(\ell) \zeta(\ell) d\ell. \quad (34)$$

To solve Eq. (33) numerically, we impose the boundary condition $\xi(\ell) \xrightarrow{\ell \rightarrow \pm\infty} 0$ and set the total length of the string $L = 1.1$. Fixing L to a particular value makes r_0 a μ and B dependent quantity. Note that $L = 1.1$ is arbitrary but as long as it lies in the unstable region, most of our results remain qualitatively the same for different values of L .

For $L = 1.1$, we have collected some r_0 values for the unstable string at different magnetic field and chemical potential values in Table I. The value of r_0 increases if we increase either the magnetic field or the chemical potential. This implies that the tip of the string moves away from the black hole horizon when we increase these parameters. There have been suggestions that the black hole can act as a source of chaos [32, 33]. If indeed this is true, we can also expect a decrease in chaos with the chemical potential and magnetic field as the tip of the string moves away from the horizon for higher values of these parameters. This expectation turns out to be true.

μ	r_0 (\parallel)	r_0 (\perp)	μ	r_0 (\parallel)	r_0 (\perp)	μ	r_0 (\parallel)	r_0 (\perp)
B = 0.0			B = 0.1			B = 0.2		
0.0	1.08318	1.08318	0.0	1.08382	1.08429	0.0	1.08581	1.08768
0.3	1.08334	1.08334	0.3	1.08398	1.08445	0.3	1.08596	1.08786
0.6	1.08386	1.08386	0.6	1.08449	1.08499	0.6	1.08647	1.08843
0.9	1.08485	1.08485	0.9	1.08547	1.08600	0.9	1.08742	1.08951
1.2	1.08657	1.08657	1.2	1.08718	1.08776	1.2	1.08908	1.09161
B = 0.3			B = 0.4			B = 0.5		
0.0	1.08940	1.09417	0.0	1.09598	1.10519	0.0	1.10728	1.12473
0.3	1.08955	1.09441	0.3	1.09615	1.10551	0.3	1.10750	1.12524
0.6	1.09004	1.09516	0.6	1.09671	1.10652	0.6	1.10818	1.12686
0.9	1.09113	1.09657	0.9	1.09778	1.10840	0.9	1.10947	1.12985
1.2	1.09302	1.09895	1.2	1.09963	1.11177	1.2	1.11202	1.13549

TABLE I. The magnitude of r_0 for the unstable string configuration is shown here for various magnetic field and chemical potential values for both parallel and perpendicular orientations. The parameter $L = 1.1$ is used, with all quantities in units of GeV.

Both eigenvalues and eigenfunctions of Eq. (33) can be obtained numerically. We collected the two lowest eigenvalues (ω_0^2 , ω_1^2) for different values of B and μ , for both parallel and perpendicular cases, in Table II. The corresponding eigenfunctions $\xi(\ell) = e_0(\ell)$ and $\xi(\ell) = e_1(\ell)$ are even and odd functions of ℓ , respectively, and are illustrated in Fig. 5. The occurrence of negative eigenvalues is a common feature of unstable systems. That is indeed the case for the unstable string, where we can see that the lowest eigenvalue is negative for all values of B and μ . This observation suggests instability of the string under perturbation. Moreover, the value of our lowest eigenvalue ω_0^2 increases if we increase either B or μ . This is true for both parallel and perpendicular string configurations. Hence, we can expect our system to stabilise if we increase these parameters. Moreover, for a fixed value of B or μ , the magnitude of ω_0^2 is more negative for the parallel case than the perpendicular one. This suggests that the magnetic field induces more instability in the string configuration in the former case compared to the latter case. Later, via the Poincaré section and Lyapunov exponent, we will see that these expectations indeed turn out to be true. Let us mention here that our results with B are different from the results of [36], where more stability was found for the parallel case compared to the perpendicular one.

Now we expand the string action up to cubic order in the perturbation. Considering only the two lowest eigenfunctions,

$$\xi(t, \ell) = c_0(t)e_0(\ell) + c_1(t)e_1(\ell), \quad (35)$$

the cubic order term of the expanded action, up to the surface terms, takes the form

$$S^{(3)} = \frac{1}{2\pi\alpha'} \int dt \int_{-\infty}^{\infty} d\ell \left(D_0^{x_i} \xi^3 + D_1^{x_i} \xi (\xi')^2 + D_2^{x_i} \xi^2 \xi' \right), \quad (36)$$

where $c_0(t)$ and $c_1(t)$ encode the perturbation's time dependence and $D_{0,1,2}^{x_i}$ are functions of ℓ . In terms of e_0 and e_1 , the above action becomes

$$S^{(3)} = \frac{1}{2\pi\alpha'} \int dt \int_{-\infty}^{\infty} d\ell \left[(e_0^3 D_0^{x_i} + D_1^{x_i} e_0 e_0'^2) c_0^3 + 3e_0 e_1^2 c_0 c_1^2 D_0^{x_i} \right. \\ \left. + (2e_0 e_1 e_1' + e_0 e_1'^2) c_0 c_1^2 D_1^{x_i} + (c_0 \dot{c}_0^2 e_0^3 + c_0 \dot{c}_1^2 e_1^2 e_0 + 2c_1 \dot{c}_0 \dot{c}_1 e_1^2 e_0) D_2^{x_i} \right]. \quad (37)$$

μ	$\omega_0^2 (\parallel)$	$\omega_1^2 (\parallel)$	μ	$\omega_0^2 (\perp)$	$\omega_1^2 (\perp)$	μ	$\omega_0^2 (\parallel)$	$\omega_1^2 (\parallel)$	μ	$\omega_0^2 (\perp)$	$\omega_1^2 (\perp)$
B = 0.0						B = 0.3					
0.0	-2.9503	5.8881	0.0	-2.9503	5.8881	0.0	-2.6448	6.0230	0.0	-2.6291	6.0307
0.3	-2.8844	5.8561	0.3	-2.8844	5.8561	0.3	-2.5884	5.9917	0.3	-2.5724	6.0034
0.6	-2.6911	5.7604	0.6	-2.6911	5.7604	0.6	-2.4229	5.8987	0.6	-2.4068	5.9221
0.9	-2.3847	5.6024	0.9	-2.3847	5.6024	0.9	-2.2036	5.7089	0.9	-2.1439	5.7893
1.2	-1.9891	5.3863	1.2	-1.9891	5.3863	1.2	-1.8119	5.5503	1.2	-1.8042	5.6114
B = 0.1						B = 0.4					
0.0	-2.9165	5.9011	0.0	-2.9155	5.9006	0.0	-2.3834	6.1918	0.0	-2.3512	6.2170
0.3	-2.8517	5.8691	0.3	-2.8508	5.8688	0.3	-2.3385	6.1621	0.3	-2.3015	6.1938
0.6	-2.6617	5.7736	0.6	-2.6607	5.7746	0.6	-2.1879	6.0742	0.6	-2.1558	6.1251
0.9	-2.4110	5.5798	0.9	-2.3598	5.6186	0.9	-1.9554	5.9299	0.9	-1.9246	6.0417
1.2	-2.0498	5.3305	1.2	-1.9710	5.4058	1.2	-1.6527	5.7349	1.2	-1.6221	5.8790
B = 0.2						B = 0.5					
0.0	-2.8151	5.9427	0.0	-2.8121	5.9394	0.0	-2.0131	6.5095	0.0	-1.9275	6.6160
0.3	-2.7537	5.9108	0.3	-2.7506	5.9090	0.3	-1.9716	6.4825	0.3	-1.8855	6.6001
0.6	-2.5730	5.8165	0.6	-2.5707	5.8181	0.6	-1.8502	6.4016	0.6	-1.7621	6.5549
0.9	-2.2864	5.6604	0.9	-2.2852	5.6683	0.9	-1.6563	6.2700	0.9	-1.5661	6.4866
1.2	-1.9155	5.4464	1.2	-1.9127	5.4728	1.2	-1.3980	6.1060	1.2	-1.3018	6.4314

TABLE II. The first two eigenvalues, ω_0^2 and ω_1^2 , for the unstable string configuration are presented here for various magnetic field and chemical potential values for both parallel and perpendicular orientations. The parameter $L = 1.1$ is used, with all values in units of GeV.

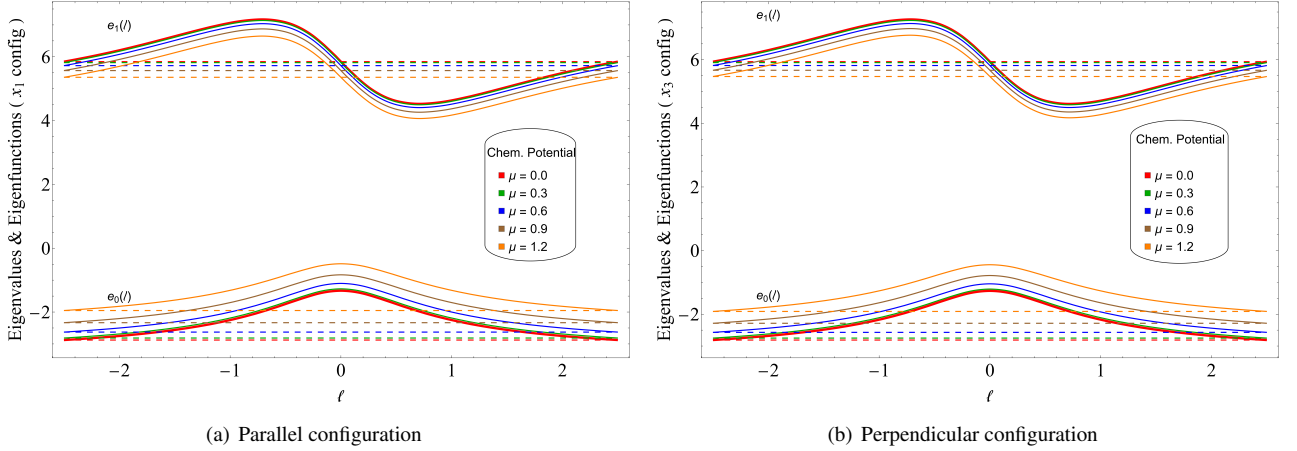


FIG. 5. The eigenfunctions $e_0(\ell)$ and $e_1(\ell)$ from Eq. (33) are shown as a function of ℓ for different values of the chemical potential for both parallel and perpendicular string configurations. The values $B = 0.2$ and $L = 1.1$ are used, with all quantities in units of GeV.

Summing $S^{(2)} + S^{(3)}$, and integrating out ℓ from the equation, we get

$$S^{(3)} + S^{(2)} = \frac{1}{2\pi\alpha'} \int dt \left[\sum_{n=0,1} (\dot{c}_n^2 - c_n^2 \omega_n^2) + c_0^3 K_1^{X_i} + c_0 c_1^2 K_2^{X_i} + c_0 \dot{c}_0^2 K_3^{X_i} + c_0 \dot{c}_1^2 K_4^{X_i} + \dot{c}_0 c_1 \dot{c}_1 K_5^{X_i} \right]. \quad (38)$$

The above action can be used to set the equation of motion for $c_0(t)$ and $c_1(t)$. The coefficients $K_{1,\dots,5}^{X_i}$ can be obtained numerically. Their values depend on the magnitude of L , B , and μ . For $L = 1.1$, the values of $K_{1,\dots,5}^{X_i}$ are collected in the table III for different values of B and μ .

Interestingly, the above action (38) contains a trapping potential for the unstable string configuration. Analysing the dynamics of c_0 and c_1 around the trapping potential is crucial to establish the stability of the string motion. However, in some parts of the potential region, the kinetic term of c_0 and c_1 in action (38) becomes negative. In order to avoid such a situation and make

μ	K_1 ()	K_2 ()	K_3 ()	K_4 ()	K_5 ()	K_1 (\perp)	K_2 (\perp)	K_3 (\perp)	K_4 (\perp)	K_5 (\perp)
B = 0.0										
0.0	9.873	12.432	5.896	2.197	4.394	9.873	12.432	5.896	2.197	4.394
0.3	9.577	12.174	5.866	2.197	4.395	9.577	12.174	5.866	2.197	4.395
0.6	8.725	11.417	5.777	2.197	4.395	8.725	11.417	5.777	2.197	4.395
0.9	7.423	10.223	5.631	2.197	4.395	7.423	10.223	5.631	2.197	4.395
1.2	5.835	8.694	5.432	2.197	4.394	5.835	8.694	5.432	2.197	4.394
B = 0.1										
0.0	9.782	12.352	5.885	2.196	4.391	9.771	12.340	5.872	2.197	4.395
0.3	9.491	12.098	5.855	2.196	4.392	9.481	12.086	5.843	2.197	4.395
0.6	8.653	11.352	5.768	2.196	4.392	8.644	11.340	5.755	2.198	4.395
0.9	7.371	10.176	5.625	2.196	4.392	7.365	10.165	5.612	2.198	4.395
1.2	5.805	8.666	5.429	2.196	4.392	5.803	8.658	5.417	2.197	4.394
B = 0.2										
0.0	9.511	12.115	5.852	2.191	4.382	9.476	12.069	5.804	2.198	4.397
0.3	9.234	11.871	5.824	2.191	4.382	9.201	11.826	5.776	2.198	4.397
0.6	8.545	11.240	5.753	2.191	4.382	8.409	11.116	5.694	2.199	4.398
0.9	7.429	10.195	5.629	2.191	4.382	7.195	9.993	5.559	2.199	4.398
1.2	5.714	8.587	5.418	2.193	4.386	5.703	8.547	5.370	2.198	4.395
B = 0.3										
0.0	9.066	11.734	5.797	2.182	4.364	8.982	11.611	5.684	2.199	4.397
0.3	8.812	11.509	5.772	2.182	4.365	8.730	11.385	5.658	2.199	4.397
0.6	8.078	10.848	5.695	2.184	4.367	8.005	10.726	5.581	2.199	4.397
0.9	6.942	9.795	5.566	2.185	4.369	6.893	9.686	5.456	2.198	4.397
1.2	5.545	8.440	5.389	2.185	4.371	5.527	8.354	5.287	2.198	4.396
B = 0.4										
0.0	8.414	11.182	5.697	2.165	4.329	8.293	10.961	5.510	2.197	4.393
0.3	8.189	10.980	5.675	2.165	4.330	8.073	10.760	5.487	2.197	4.393
0.6	7.540	10.390	5.607	2.167	4.334	7.440	10.175	5.420	2.197	4.393
0.9	6.536	9.452	5.494	2.169	4.339	6.467	9.251	5.310	2.196	4.393
1.2	5.292	8.238	5.341	2.172	4.345	5.262	8.062	5.159	2.195	4.391
B = 0.5										
0.0	7.552	10.485	5.543	2.134	4.268	7.378	10.074	5.261	2.187	4.373
0.3	7.364	10.314	5.524	2.135	4.270	7.196	9.905	5.242	2.186	4.373
0.6	6.819	9.810	5.467	2.137	4.275	6.674	9.410	5.185	2.186	4.373
0.9	5.972	9.008	5.374	2.141	4.283	5.869	8.629	5.094	2.186	4.372
1.2	4.907	7.960	5.241	2.145	4.290	4.864	7.621	4.964	2.184	4.368

TABLE III. The K values are depicted for various μ and B values for both parallel and perpendicular string orientations within the string frame. The parameter $L = 1.1$ is used, with all quantities expressed in units of GeV.

the kinetic term positive definite, we transform $c_{0,1} \rightarrow \tilde{c}_{0,1}$, where $c_0 = \tilde{c}_0 + \alpha_1 \tilde{c}_0^2 + \alpha_2 \tilde{c}_1^2$ and $c_1 = \tilde{c}_1 + \alpha_3 \tilde{c}_0 \tilde{c}_1$, following the strategy adopted in [32–34]. Now, the values of α_1 , α_2 , and α_3 can be chosen to get rid of the negative kinetic situation. One such choice for α 's are $\alpha_1 = -1.35$, $\alpha_2 = -0.5$, and $\alpha_3 = -1$. Using the modified values, our action becomes

$$S^{(\text{modified})} = \frac{1}{2\pi\alpha'} \int dt \left[\sum_{n=0,1} (\dot{\tilde{c}}_n^2 - \tilde{c}_n^2 \omega_n^2) + \tilde{c}_0^3 \tilde{K}_1^{x_i} + \tilde{c}_0 \tilde{c}_1^2 \tilde{K}_2^{x_i} + \tilde{c}_0 \tilde{c}_0^2 \tilde{K}_3^{x_i} + \tilde{c}_0 \tilde{c}_1^2 \tilde{K}_4^{x_i} + \dot{\tilde{c}}_0 \tilde{c}_1 \dot{\tilde{c}}_1 \tilde{K}_5^{x_i} \right]. \quad (39)$$

The above transformation makes the time evolution of c_0 and c_1 well-posed without affecting their dynamics. In addition to that the chaotic structure also shows up in the modified action. From the modified action we can further find out the equations of

motion of \tilde{c}_0 and \tilde{c}_1

$$\begin{aligned} \ddot{\tilde{c}}_0 = & - \frac{1}{4(\tilde{c}_0(4\alpha_1 + K_3) + 1)(\tilde{c}_0(2\alpha_3 + K_4) + 1) - \tilde{c}_1^2(4\alpha_2 + 2\alpha_3 + K_5)^2} \\ & \times (2\tilde{c}_0(2\alpha_3 + K_4) + 2)(4\alpha_1\tilde{c}_0^2 + 4\alpha_2\tilde{c}_1^2 - 3\tilde{c}_0^2(K_1 - 2\alpha_1\omega_0^2) \\ & + \tilde{c}_1^2(2\alpha_2\omega_0^2 + 2\alpha_3\omega_1^2 - K_2) + \tilde{c}_0^2K_3 - \tilde{c}_1^2K_4 + \tilde{c}_1^2K_5 + 2\tilde{c}_0\omega_0^2) \\ & - 2\tilde{c}_1(4\alpha_2 + 2\alpha_3 + K_5)(\tilde{c}_0\tilde{c}_1(2\alpha_2\omega_0^2 + 2\alpha_3\omega_1^2 - K_2) + \dot{\tilde{c}}_0\dot{\tilde{c}}_1(2\alpha_3 + K_4) + \tilde{c}_1\omega_1^2), \end{aligned} \quad (40)$$

$$\begin{aligned} \ddot{\tilde{c}}_1 = & \frac{1}{4\tilde{c}_0^2(4\alpha_1 + K_3)(2\alpha_3 + K_4) + 4\tilde{c}_0(4\alpha_1 + 2\alpha_3 + K_3 + K_4) - \tilde{c}_1^2(4\alpha_2 + 2\alpha_3 + K_5)^2 + 4} \\ & (\tilde{c}_1^3(4\alpha_2 + 2\alpha_3 + K_5)(2\alpha_2\omega_0^2 + 2\alpha_3\omega_1^2 - K_2) - \tilde{c}_0^2\tilde{c}_1(8\alpha_1\alpha_2\omega_0^2 - 12\alpha_1\alpha_3\omega_0^2 + 32\alpha_1\alpha_3\omega_1^2 \\ & - 6\alpha_1K_5\omega_0^2 + 8\alpha_2K_3\omega_0^2 + 8\alpha_3K_3\omega_1^2 - 4K_2(4\alpha_1 + K_3) + 3K_1(4\alpha_2 + 2\alpha_3 + K_5)) \\ & + \tilde{c}_1(\tilde{c}_0^2(4\alpha_1 + K_3)(4\alpha_2 + 2\alpha_3 + K_5) - \tilde{c}_1^2(-4\alpha_2 + K_4 - K_5) \\ & \times (4\alpha_2 + 2\alpha_3 + K_5) - 4\omega_1^2) + 2\tilde{c}_0(\tilde{c}_1(2\alpha_3\omega_0^2 - 8\alpha_1\omega_1^2 - 4\alpha_3\omega_1^2 + K_5\omega_0^2 - 2K_3\omega_1^2 + 2K_2) \\ & - 2\dot{\tilde{c}}_0\dot{\tilde{c}}_1(4\alpha_1 + K_3)(2\alpha_3 + K_4)) - 4\dot{\tilde{c}}_0\dot{\tilde{c}}_1(2\alpha_3 + K_4)). \end{aligned} \quad (41)$$

We have written down these equations of motion explicitly as they will be useful later on in the analysis of the Lyapunov exponent at the unstable fixed point.

C. Poincaré sections

Poincaré sections are used to better observe the qualitative nature of chaotic dynamics. Although we can not use it to quantify the chaos of string dynamics (which can be done using the Lyapunov exponents, see the next subsection III D), we can get information about where the chaotic behaviour of the string emerges via the Poincaré section. We take our equation of motion and trace out in the phase space with time as the parameter and construct the Poincaré section for bound orbits with the section identified by $\tilde{c}_1(t) = 0$ and $\dot{\tilde{c}}_1(t) \geq 0$ in the phase space. The conditions $\{\tilde{c}_1(t) = 0, \dot{\tilde{c}}_1(t) \geq 0\}$ correspond to bound orbits within the trapping potential. To obtain the Poincaré sections we start with various initial conditions with fixed energy $E = 10^{-5}$ and time interval $0 < t < 15000$. This energy is chosen for illustrative purposes.

Fig. 6 shows a close-up profile of the Poincaré section near the origin, where most of the interesting things happen, both for parallel and perpendicular string configurations. Here $B = 0.2$ and $\mu = 0, 0.3, 0.6, 0.9,$ and 1.2 are used for illustrative purposes. The choice of $B = 0.2$ is arbitrary, in the sense that it is chosen just to demonstrate the anisotropic chaotic nature of the string as we vary the value of μ . The data points in different colours correspond to numerical data of orbits for different starting conditions.

We find from the Poincaré sections that for both x_1 (\parallel) and x_3 (\perp) cases the chaos shows up only near the black hole event horizon. We observe scattered points concentrating near the origin $\tilde{c}_0 \simeq 0$, showing strong dependence on initial conditions. These scattered points convert into regular paths for higher values of B and μ . This suggests that the effect of the magnetic field and chemical potential is to reduce the chaotic behaviour. This is true for both parallel and perpendicular configurations of the string. Referring to Table I, we can see that as the chemical potential increases, the tip of the unstable string r_0 moves away from the horizon, although the change in r_0 with the chemical potential is small as compared to the changes by the magnetic field. This implies that the chaos's source is the black hole's event horizon. The same behaviour was observed in [32].

We can also observe that the nature of the chaos is quite different between the x_1 and x_3 configurations of the string. The chaos in the perpendicular configuration is less compared to the parallel configuration. This analysis makes sense if we look at Table I again. We can see that at the same magnetic field value, the tip of the string is farther away from the horizon for the perpendicular than for the parallel configuration. Hence less chaos is expected in the former case compared to the latter. We would like to again point out that the chaos is significant only when the unstable string is near the horizon irrespective of the magnetic configuration. For instance, for the stable string (i.e., the large r_0 solution), which is relatively far from the horizon, there are only stable orbits without scattered points, suggesting no chaos for the stable string configuration for any values of B and μ .

Although the Poincaré section is quite helpful in identifying the chaotic "position" in the phase space, the inability to give a quantitative result makes it difficult for us to compare the chaos between different configurations. For this reason, we will move on to the analysis of our system using the Lyapunov exponents.

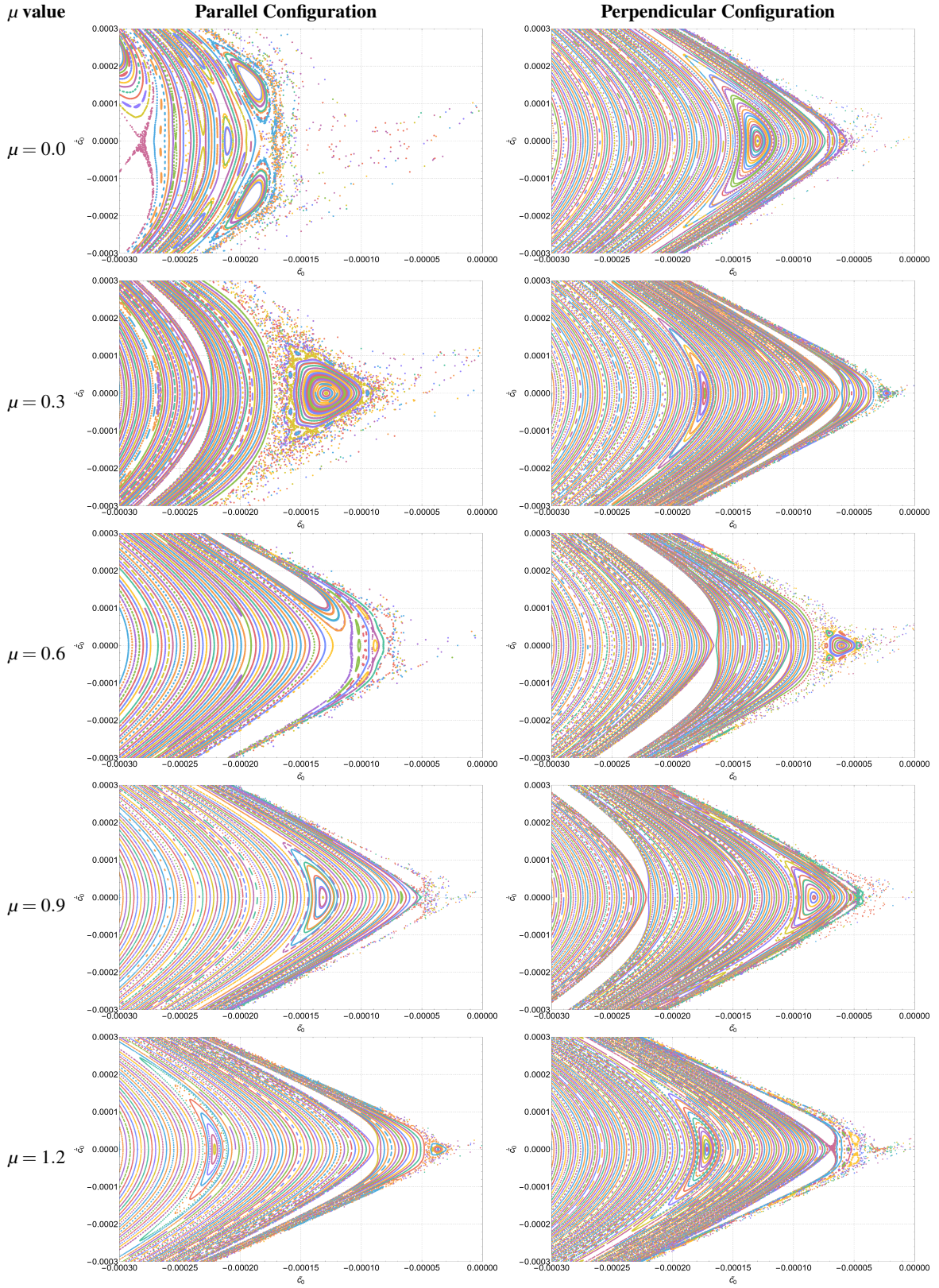


FIG. 6. The Poincaré sections are shown for different values of μ , with the left figure representing the x_1 (parallel) string configuration and the right figure representing the x_3 (perpendicular) configuration. Each section is identified by $\tilde{c}_1(t) = 0$ and $\dot{\tilde{c}}_1(t) \geq 0$ with $E = 10^{-5}$. The parameters $L = 1.1$ and $B = 0.2$ are fixed, with all quantities in units of GeV.

D. Lyapunov exponents

Lyapunov exponents can be used to quantitatively analyse chaotic dynamics in classical mechanics. We numerically compute the Lyapunov exponent in the four-dimensional phase space $(\tilde{c}_0, \tilde{c}_1)$ using methods given in [142, 143]. As before, we focus on the system with $L = 1.1$ and energy $E = 10^{-5}$ for both the x_1 and x_3 orientations of the string. Fig. 7, shows the convergence diagram of the four Lyapunov exponents. The behaviour is that of a damped oscillation, although we cannot make that observation from our figure due to the high-resolution nature of the plots. In the previous subsection III C, we discussed the results of the Poincaré section analysis (Fig. 6) for various μ values and fixed $B = 0.2$. To create the necessary data on the quantitative nature of the chaos, we also extract the Lyapunov exponents for similar values of B and μ in Fig. 7. In our calculation, we took 8×10^5 time steps with step size 0.001, making our analysis numerically sufficiently accurate. Also, we have taken the coefficients $K_{1,\dots,5}^{x_i}$ up to a 10^{-3} level of accuracy. We did not find any substantial effect when enforcing greater accuracy.

From our action (39), we can already see that there will be four Lyapunov exponents, which we represent in different colours in each graph. We have computed the convergency plots of these four Lyapunov coefficients and their sum. The behaviour of each exponent is that of a damped oscillation. The sum of the Lyapunov exponents converges to zero at later times, suggesting the conservative nature of the system. This can be explicitly observed from the last row of Fig. 7. The same structure is present for all values of B and μ , irrespective of the orientation of the string concerning the magnetic field.

The maximal Lyapunov exponent, denoted as λ_{max} , can be extrapolated from various configurations by considering sufficient time steps and fitting the maximum in each oscillation. The obtained λ_{max} results are shown in Fig. 8 for parallel and perpendicular cases for different values of the chemical potential and magnetic field. Here the string length $L = 1.1$ is kept fixed for all cases. It is observed that λ_{max} decreases for both orientations of the string as μ or B increases. Additionally, for fixed values of B and μ , λ_{max} is smaller in the perpendicular case compared to the parallel one. The Poincaré section analysis supported such observation already in the previous section. We further observe that the Lyapunov exponent decreases sharply as μ increases starting from 0.6 for lower magnetic field values, i.e., $B = 0.0, 0.1$ and 0.2 for both the x_1 and x_3 configurations. This indicates a rapid stabilisation of the system by the chemical potential at a lowering of the magnetic field. But this rapid stabilisation vanishes as the magnetic field B increases. Our overall Lyapunov exponent analysis confirms more qualitatively that the string dynamics become less chaotic when the chemical potential or magnetic field increases for both parallel and perpendicular string orientations.

Our choice of the string length $L = 1.1$ is still arbitrary. As long as we stick to the unstable area of the system, i.e., r_0 near the horizon, we have already seen that the chaotic nature is only significant near the black hole horizon.

E. Saddle point analysis and MSS bound

μ	\tilde{c}_0 (\parallel)	\tilde{c}_0 (\perp)	μ	\tilde{c}_0 (\parallel)	\tilde{c}_0 (\perp)	μ	\tilde{c}_0 (\parallel)	\tilde{c}_0 (\perp)
B = 0.0			B = 0.1			B = 0.2		
0.0	-1.0313	-1.0313	0.0	-1.0196	-1.0231	0.0	-0.9826	-0.9952
0.3	-1.0746	-1.0746	0.3	-1.0614	-1.0652	0.3	-1.0202	-1.0332
0.6	-1.2293	-1.2293	0.6	-1.2101	-1.2145	0.6	-1.1519	-1.1672
0.9	-1.6141	-1.6141	0.9	-1.5765	-1.5827	0.9	-1.4654	-1.4860
1.2	-2.8563	-2.8563	1.2	-2.7184	-2.7301	1.2	-2.3554	-2.3682
B = 0.3			B = 0.4			B = 0.5		
0.0	-0.9158	-0.9307	0.0	-0.8030	-0.8061	0.0	-0.6339	-0.5912
0.3	-0.9465	-0.9610	0.3	-0.8240	-0.8252	0.3	-0.6441	-0.5969
0.6	-1.0516	-1.0646	0.6	-0.8936	-0.8873	0.6	-0.6766	-0.6130
0.9	-1.2852	-1.2941	0.9	-1.0374	-1.0100	0.9	-0.7363	-0.6364
1.2	-1.8500	-1.8337	1.2	-1.3285	-1.2258	1.2	-0.8230	-0.6432

TABLE IV. The location of the minima point $(\tilde{c}_0, \tilde{c}_1 = 0)$ is shown for various values of the magnetic field and chemical potential for both parallel and perpendicular orientations. The parameter $L = 1.1$ is used, with all quantities expressed in units of GeV.

It is clear from the previous analysis that the dynamics of the string produces positive values for the largest Lyapunov exponents, suggesting chaos in its dynamics. In order to make our discussion complete, in this section, we will analyse the Lyapunov exponent at the unstable fixed points and make a comparison with the MSS bound. The potential in the action (39) gives rise to two fixed points, a stable and an unstable one. The former corresponds to the minimum of the potential, while the latter to the

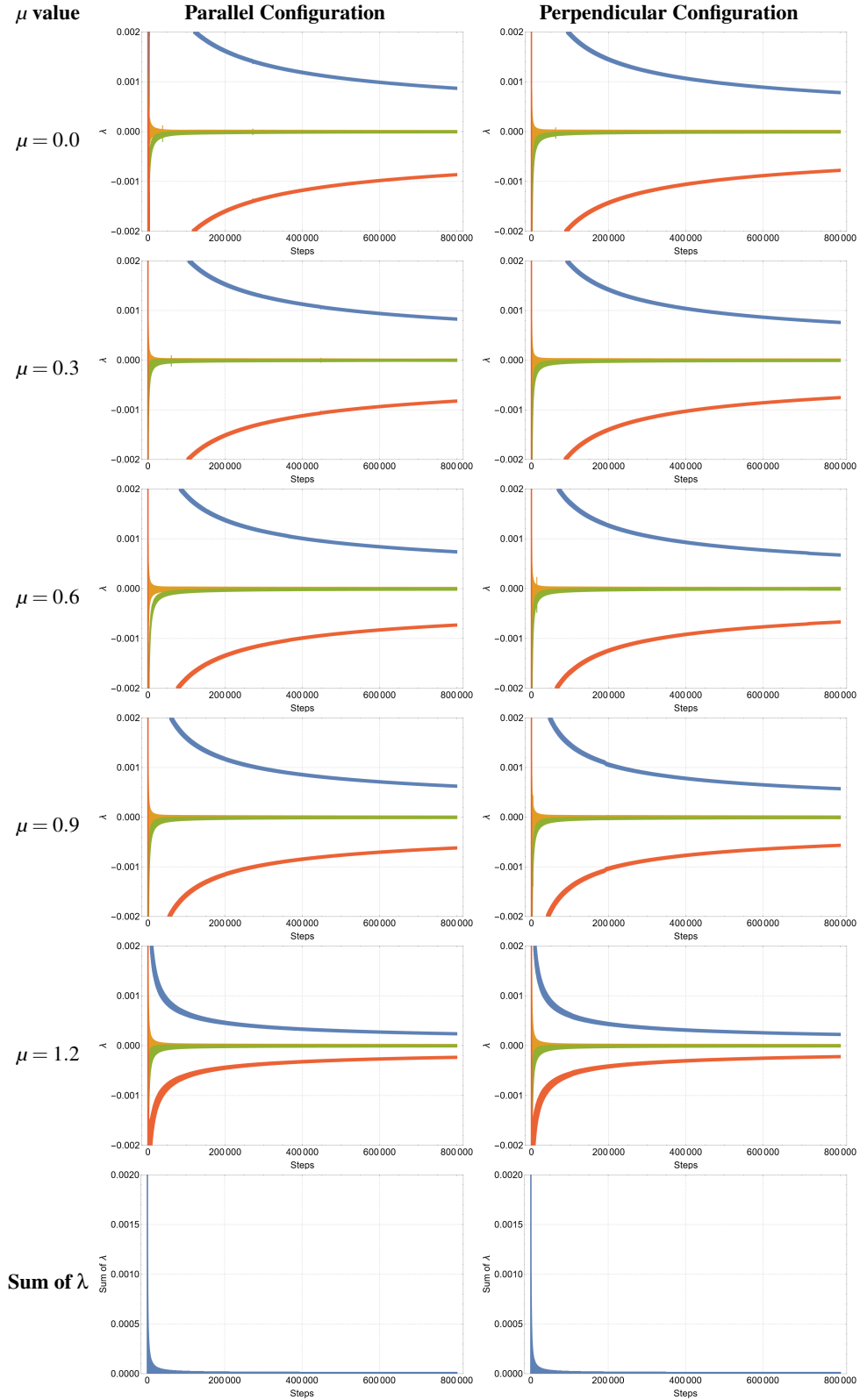


FIG. 7. Convergence plots of the four Lyapunov exponents are displayed for different values of μ , with the string oriented parallel (left column) and perpendicular (right column) to the magnetic field. The last row shows the sum of the Lyapunov exponents for $\mu = 0.6$ and $B = 0.2$. Similar converging behaviour is observed for all values of the magnetic field and chemical potential. Here the initial conditions $\tilde{c}_0 = -0.0003$, $\tilde{c}_1(t) = 0.00001$, and $\tilde{c}_1 = 0.0008$ are used for both the configurations. The parameters $L = 1.1$, $E = 10^{-5}$, and $B = 0.2$ are fixed, with all quantities in units of GeV.

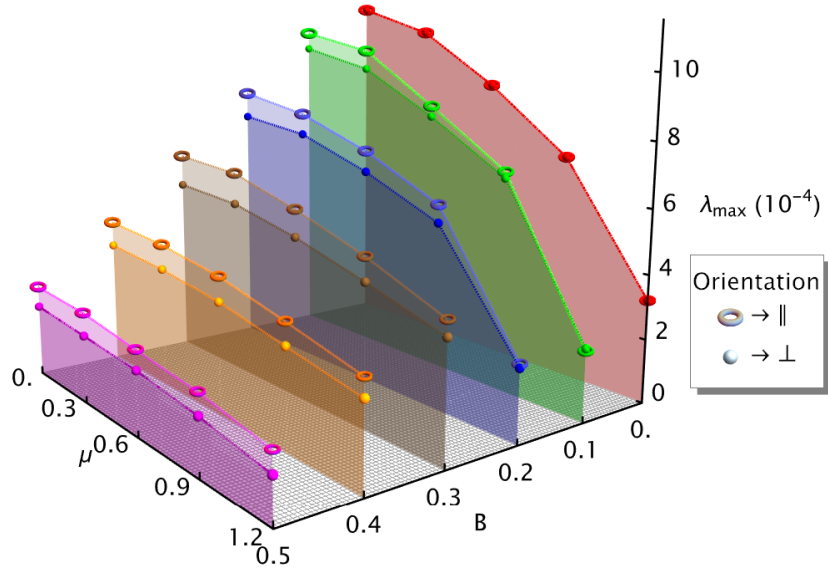


FIG. 8. The maximum Lyapunov exponent λ_{\max} is compared for the x_1 (\parallel) and x_3 (\perp) orientations of the string at various values of B and μ , close to the unstable saddle point. Data points are colour-coded as follows: red, green, blue, brown, orange, and magenta colours represent $B = 0.0, 0.1, 0.2, 0.3, 0.4,$ and 0.5 , respectively. The string length is fixed at $L = 1.1$, and $E = 10^{-5}$.

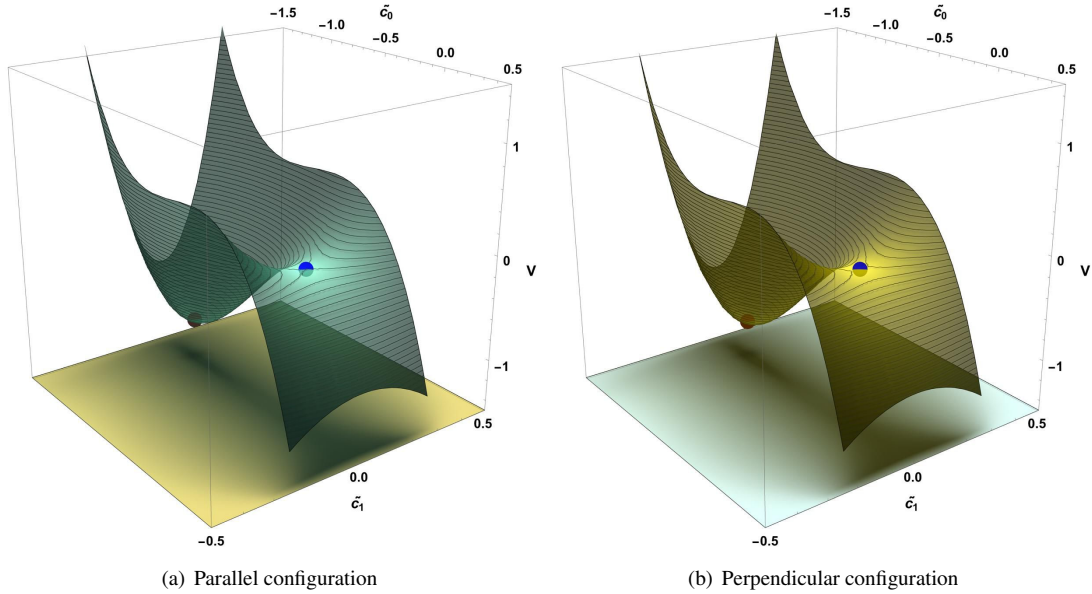


FIG. 9. A three-dimensional plot of the potential is shown, with the red dot indicating the local minima and the blue dot representing the saddle point. The parameters used are $B = 0.2$, $\mu = 0.6$, and $L = 1.1$, with all values expressed in units of GeV.

saddle point. These fixed points are explicitly shown in Fig. 9, where the red dot corresponds to the local minima and the blue dot corresponds to the saddle point of the potential. These two fixed points are similar in positioning and appearance for both x_1 and x_3 configurations.

The entire evolution of the system given in (39) is governed by $\vec{y}' = \vec{F}$, where $\vec{y} = (\tilde{c}_0, \dot{\tilde{c}}_0, \tilde{c}_1, \dot{\tilde{c}}_1)$. The two fixed points correspond to $\vec{F} = 0$. For energy $E = 0$, the saddle point is found at the location $\vec{y} = (0, 0, 0, 0)$ for the unstable string. Interestingly, the saddle point is always located at $\vec{y} = (0, 0, 0, 0)$ for all values of B and μ . Whereas the position of the local minimum changes with B and μ . In particular, the location of the minimum, specified by $(\tilde{c}_0, \tilde{c}_1 = 0)$, moves further away from the saddle point as B and μ increases. The precise location of the minimum is specified in Table IV for different B and μ values.

We numerically obtain the Lyapunov exponents at the saddle point $\vec{y} = (0, 0, 0, 0)$ in a similar way as in the last section and

find that they asymptotically converge to $(\sqrt{-\omega_0^2}, -\sqrt{-\omega_0^2}, 0, 0)$, where the eigenvalues ω_0^2 are given in Table II. Therefore, the largest Lyapunov exponent at the saddle point is $\lambda_{max} = \sqrt{-\omega_0^2}$. Accordingly, the largest Lyapunov exponent decreases with B and μ for both parallel and perpendicular string orientation.

Interestingly, we can also obtain the Lyapunov exponents analytically at the saddle point. In particular, at the saddle point, the Lyapunov exponents are given by the real part of the eigenvalues of the Jacobian matrix of \vec{F} [142]. At the saddle point, the Jacobian matrix (J) is of the form

$$J = \begin{pmatrix} 0 & -\omega_0^2 & 0 & 0 \\ 1 & 0 & 0 & 0 \\ 0 & 0 & 0 & -\omega_1^2 \\ 0 & 0 & 1 & 0 \end{pmatrix}, \quad (42)$$

and its eigenvalues are $(-i\sqrt{\omega_0^2}, i\sqrt{\omega_0^2}, -i\sqrt{\omega_1^2}, i\sqrt{\omega_1^2})$. Since $\omega_0^2 < 0$ and $\omega_1^2 > 0$, we have two non-zero Lyapunov exponent $(\sqrt{-\omega_0^2}, -\sqrt{-\omega_0^2}, 0, 0)$, with largest Lyapunov exponent being $\lambda_{max} = \sqrt{-\omega_0^2}$. This is the same expression that we obtained earlier at the saddle point. This further advocates for the correctness of the numerical routine, and hence the corresponding numerical results, considered in this work.

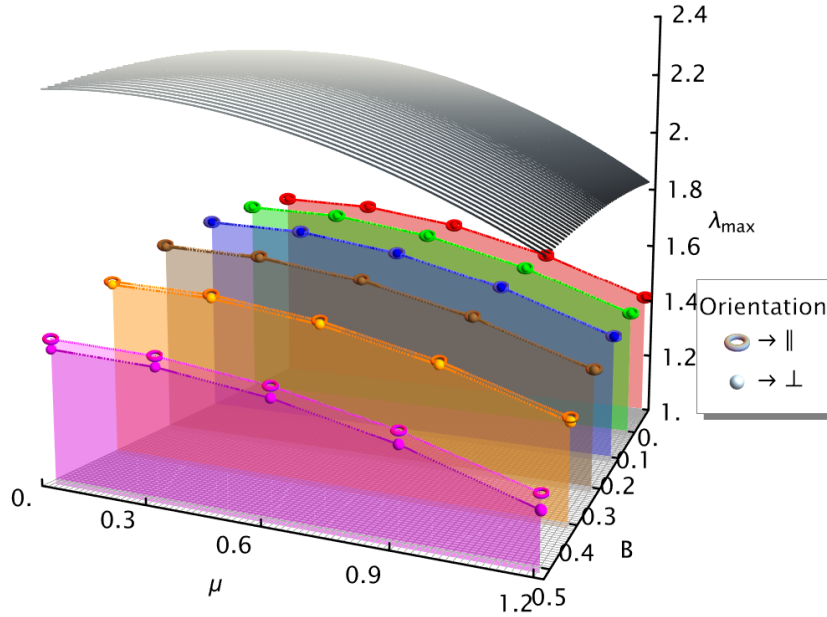


FIG. 10. The comparison of the maximum Lyapunov exponent λ_{max} and the MSS bound is presented for the x_1 (\parallel) and x_3 (\perp) orientations at the unstable saddle point. Data points are colour-coded as follows: red, green, blue, brown, orange, and magenta colours represent $B = 0.0, 0.1, 0.2, 0.3, 0.4,$ and 0.5 , respectively. The MSS bound is indicated by the grey surface above the data points.

It is also important to compare the obtained Lyapunov exponents with the MSS bound. The MSS bound, from Eq. (5) is given by

$$\lambda_{MSS} = \frac{r_h^2 g'(r_h)}{2}. \quad (43)$$

We find that the largest Lyapunov exponent at the saddle point is always smaller than λ_{MSS} for all B and μ values, suggesting that it always satisfies the MSS bound for all values of chemical potential and magnetic field irrespective of its orientation with the respect to the string. The comparison between λ_{max} and λ_{MSS} is shown in Fig. 10.

In summary, our investigation of the string frame suggests that chaos is produced in the proximity of the black hole horizon, and the role of the chemical potential and magnetic field is to weaken the dependence of the system dynamics on the initial condition, thereby making the system less chaotic. In the context of holographic QCD, this indicates that less chaos is expected in the bound state of the quark-antiquark pair at higher chemical potential and magnetic field values. This might be related to

having a less easy deconfinement, see also [33] where chaos was speculated to have a connection to the onset of deconfinement. In return, this could be related to the issue of inverse magnetic catalysis in QCD, which received a lot of attentions since the seminal lattice estimates of [144]. Although our result is true for both orientations of the string relative to the magnetic field, the string's chaotic dynamics get softened more along the transverse than the parallel direction. This could be related to the anisotropies seen in the confining properties of lattice QCD as well, see [145].

IV. CHAOTIC DYNAMICS IN THE EINSTEIN FRAME

Moving on from the string frame, we now look at how the chaotic string dynamics works out in the Einstein frame. Eq. (2) gives the corresponding black hole geometry. The dynamical analysis here is quite similar to the string frame calculation, so we can be more brief. We just need to replace the factor $A_s(r)$ by its counterpart $A(r)$. As before, our analytical framework hinges on Eqs. (11) and (12), albeit with $A_s(r) \rightarrow A(r)$. Through the application of Eqs. (20) and (21), we can extract the static string profile within the Einstein frame. Moreover, Eq. (22) gives us a means to quantify the total length of the string for both parallel and perpendicular orientations of the string.

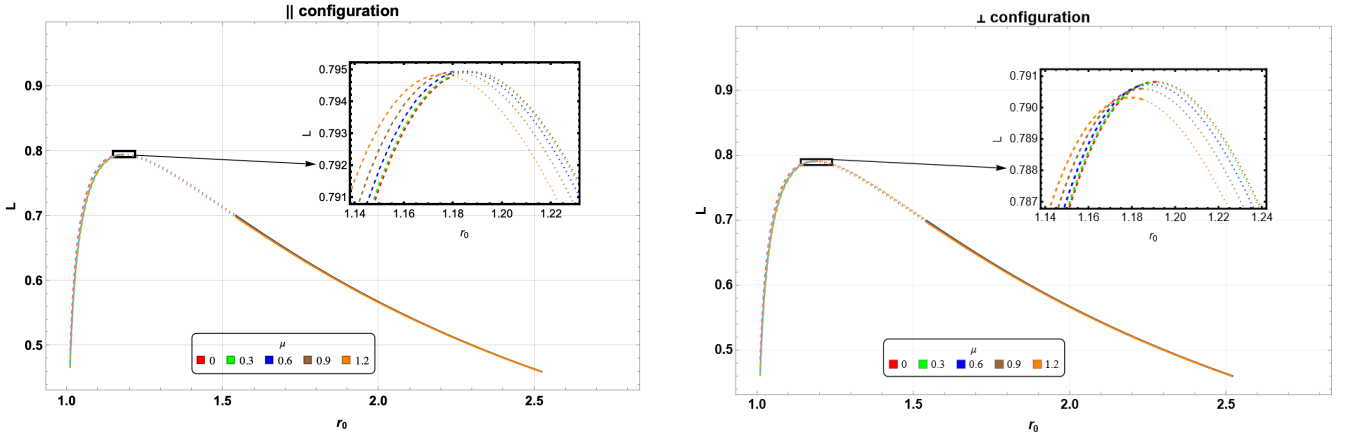


FIG. 11. Behavior of the string length L as a function of r_0 for parallel (left) and perpendicular (right) orientations of the string, with varying chemical potential μ and a fixed magnetic field $B = 0.2$. All quantities are expressed in units of GeV.

μ	r_0 (\parallel)	r_0 (\perp)	μ	r_0 (\parallel)	r_0 (\perp)	μ	r_0 (\parallel)	r_0 (\perp)
B = 0.0			B = 0.1			B = 0.2		
0.0	1.08235	1.08235	0.0	1.08214	1.08351	0.0	1.08149	1.08693
0.3	1.08178	1.08178	0.3	1.08157	1.08296	0.3	1.08091	1.08643
0.6	1.08003	1.08003	0.6	1.07984	1.08126	0.6	1.07929	1.08487
0.9	1.07752	1.07752	0.9	1.07732	1.07857	0.9	1.07672	1.08209
1.2	1.07358	1.07358	1.2	1.07336	1.07475	1.2	1.07267	1.07818
B = 0.3			B = 0.4			B = 0.5		
0.0	1.08037	1.09303	0.0	1.07896	1.10255	0.0	1.07710	1.11701
0.3	1.07981	1.09250	0.3	1.07846	1.10204	0.3	1.07657	1.11658
0.6	1.07833	1.09085	0.6	1.07692	1.10045	0.6	1.07495	1.11528
0.9	1.07568	1.08831	0.9	1.07415	1.09809	0.9	1.07204	1.11300
1.2	1.07150	1.08464	1.2	1.06984	1.09461	1.2	1.06803	1.10964

TABLE V. The parameter r_0 of the unstable string configuration for various magnetic field strengths and chemical potentials, for both parallel and perpendicular string orientations. The string length is set to $L = 0.75$. All values are given in units of GeV.

The variation of the string length $L(r_0)$ for different values of μ and $B = 0.2$ for parallel and perpendicular configurations is shown in Fig. 11. The dashed line in the figure gives the unstable string profile, solid lines give the stable profile and the dotted line denotes the meta-stable profile. Similar to what we observed in the string frame, here in the Einstein frame, we also find a

maximum length for the string, denoted as L_{max} , beyond which no connected solution of the string exists. Below L_{max} , there are two distinct types of connected string solutions: one closer to the black hole horizon (shown by dashed lines) and another further away from the horizon (represented by dotted and solid lines). The small r_0 solution again corresponds to the local maximum of the energy, whereas the large r_0 solution corresponds to the local minimum. The free energy of the string is observed to be similar to that of Fig. 3, i.e., there is a phase transition from the large r_0 connected solution to the parallel disconnected strings as the length of the string is varied, with the connected (large r_0) solution always corresponding to the stable and the disconnected one (small r_0) to the unstable configuration.

An important quantity of interest is again the tip (r_0) of the unstable string. For fixed string length $L = 0.75$, the variation of r_0 for different B and μ is given in Table V. In the subsequent analysis, we will be maintaining this fixed string length. Here, we can already appreciate some subtle differences with the string frame case. Indeed, as we increase the chemical potential, the r_0 value decreases for both the parallel (x_1) and perpendicular (x_3) orientations of the string, i.e., the tip of the string moves toward the horizon, in contrast to the string frame findings. Similarly, for a fixed μ , the value of r_0 decreases as B increases in the x_1 direction while it increases as B increases in the x_3 direction. This already suggests that not only substantial changes might appear in the chaotic dynamics of the string in terms of the chemical potential, but also magnetic field-dependent anisotropy may appear in the chaotic string dynamics in the Einstein frame. In particular, the chaotic structure might now lessen/enhance with magnetic fields in the perpendicular/parallel directions.

A. Perturbing the string

We now move on to analyse the perturbed string dynamics in the Einstein frame following the same procedure as in the string frame. Again, we are only interested in the unstable string (given by the dashed line in Fig. 11), where r_0 is closer to the horizon, as the stable string profiles do not show any chaos.

The relevant equations take the same form as in Eq. (25) and (26), thence the analysis will be very similar. We expand the action up to the second and third order in the perturbation parameter. The dynamics can then be obtained from the second-order action [see Eq. (30)], which is again of the Sturm-Liouville form [given by Eq. (33)], with coefficients $C_{\ell\ell}^{x_i}$, $C_{00}^{x_i}$ and $C_{ll}^{x_i}$. After factorizing the equation of motion, we can determine the two lowest eigenvalues and the eigenfunction of the Sturm-Liouville equation. Table VI gives us the two lowest eigenvalues for both x_1 and x_3 orientations. The lowest eigenvalue ω_0^2 is again negative for all values of μ and B , suggesting chaos in the Einstein frame as well. This is true for both x_1 and x_3 orientations of the string. Moreover, the nature of ω_0^2 is again quite similar to the string frame case. In particular, it decreases with the magnetic field and is stronger in the perpendicular direction. A similar trend can also be observed with the chemical potential. The two lowest eigenfunctions are shown in Fig. 12, which again exhibits qualitatively similar features as in the string frame case.

The perturbed action up to the third order (see Eq. (38)) can be used to determine the form of potential and the dynamics of c_0 and c_1 . This term also gives us a trapping potential in the Einstein frame. The values of the coefficient $K_{1,\dots,5}^{x_i}$ are given in the Table VII. Although the values are recorded only up to the third decimal, higher accurate values have been used in numerical computations. Similar to the string frame, to avoid a negative kinetic term in some parts of the parameter space, we transformed the parameters $c_{0,1} \rightarrow \tilde{c}_{0,1}$, where $c_0 = \tilde{c}_0 + \alpha_1 \tilde{c}_0^2 + \alpha_2 \tilde{c}_1^2$ and $c_1 = \tilde{c}_1 + \alpha_3 \tilde{c}_0 \tilde{c}_1$ following similar methods adopted in [32, 33, 36], where for the current case e.g. $\alpha_1 = -3$, $\alpha_2 = -1$, and $\alpha_3 = -1.5$ are good choices.

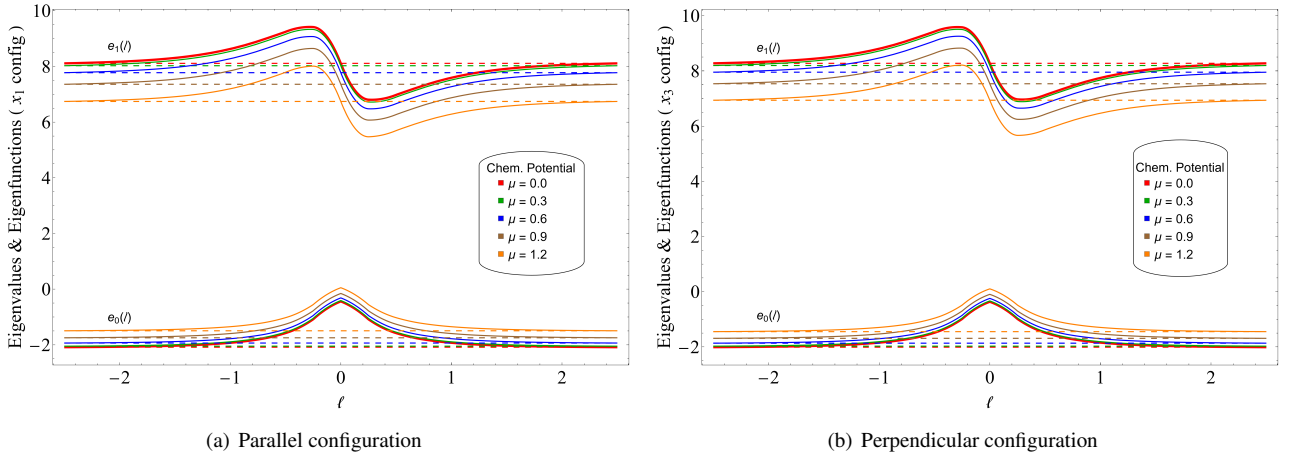


FIG. 12. The eigenfunctions $e_0(\ell)$ and $e_1(\ell)$ as a function of ℓ for different values of the chemical potential for both parallel and perpendicular string configurations. The magnetic field is set at $B = 0.2$ and the string length is set at $L = 0.75$. All values in GeV units.

μ	$\omega_0^2 (\parallel)$	$\omega_1^2 (\parallel)$	μ	$\omega_0^2 (\perp)$	$\omega_1^2 (\perp)$	μ	$\omega_0^2 (\parallel)$	$\omega_1^2 (\parallel)$	μ	$\omega_0^2 (\perp)$	$\omega_1^2 (\perp)$
B = 0.0						B = 0.3					
0.0	-2.1182	8.2144	0.0	-2.1182	8.2144	0.0	-2.0454	7.9744	0.0	-1.8794	8.3604
0.3	-2.0799	8.1291	0.3	-2.0799	8.1291	0.3	-2.0099	7.8920	0.3	-1.8472	8.2828
0.6	-1.9660	7.8695	0.6	-1.9660	7.8695	0.6	-1.8992	7.6524	0.6	-1.7518	8.0458
0.9	-1.7688	7.4501	0.9	-1.7688	7.4501	0.9	-1.7201	7.2393	0.9	-1.5898	7.6552
1.2	-1.5063	6.8297	1.2	-1.5063	6.8297	1.2	-1.4814	6.6270	1.2	-1.3689	7.0929
B = 0.1						B = 0.4					
0.0	-2.1099	8.1884	0.0	-2.0905	8.2306	0.0	-1.9856	7.7916	0.0	-1.6924	8.5113
0.3	-2.0719	8.1034	0.3	-2.0525	8.1469	0.3	-1.9511	7.7138	0.3	-1.6648	8.4387
0.6	-1.9586	7.8455	0.6	-1.9400	7.8918	0.6	-1.8486	7.4770	0.6	-1.5833	8.2169
0.9	-1.7634	7.4271	0.9	-1.7506	7.4673	0.9	-1.6831	7.0680	0.9	-1.4430	7.8557
1.2	-1.5035	6.8080	1.2	-1.4911	6.8581	1.2	-1.4610	6.4642	1.2	-1.2531	7.3336
B = 0.2						B = 0.5					
0.0	-2.0855	8.1091	0.0	-2.0114	8.2745	0.0	-1.9098	7.5516	0.0	-1.4408	8.7752
0.3	-2.0767	8.0564	0.3	-1.9746	8.1951	0.3	-1.8788	7.4746	0.3	-1.4179	8.7107
0.6	-1.9360	7.7742	0.6	-1.8662	7.9526	0.6	-1.7863	7.2411	0.6	-1.3496	8.5158
0.9	-1.7470	7.3577	0.9	-1.6905	7.5345	0.9	-1.6368	6.8376	0.9	-1.2389	8.1830
1.2	-1.4953	6.7409	1.2	-1.4481	6.9364	1.2	-1.4277	6.2673	1.2	-1.0888	7.7030

TABLE VI. The first two eigenvalues, ω_0^2 and ω_1^2 , of the unstable string configuration as a function of magnetic field strength and chemical potential for both parallel and perpendicular string orientations. The string length is fixed at $L = 0.75$. All quantities are in units of GeV.

B. Poincaré sections

Next, we study the Poincaré section in the Einstein frame for bound orbits with the section identified by $\tilde{c}_1(t) = 0$ and $\dot{\tilde{c}}_1(t) \geq 0$ in the phase space. We utilize our equation of motion and trace trajectories in the phase space using time as the parameter. Our numerical results for the Poincaré sections near the origin for different values of the chemical potential are shown in Fig. 13 for both parallel and perpendicular configurations of the string. Here we have used a fixed string length $L = 0.75$, magnetic field $B = 0.2$, and energy $E = 10^{-5}$ with $t \leq 15,000$. In the figure, different colours denote orbits with different initial conditions.

From Fig. 13, we can observe some interesting behaviour of the Poincaré sections as the chemical potential increases. In particular, there is an increase in scatter points near the origin \tilde{c}_0 for higher values of μ , indicating strong dependence on the initial conditions. This is again true for both string orientations, suggesting that turning on the chemical potential increases the chaotic behaviour. This result should be contrasted with the string frame result, where an increased chemical potential resulted in a decreased chaos for both string orientations. Similarly, though not explicitly presented here for brevity, we find that for higher values of the magnetic field, the number of scatter points amplify in the system for the parallel configuration, whereas the points order themselves into regular paths for the perpendicular configuration. This suggests that the effect of switching on the magnetic field is to aggravate the chaotic behaviour in the parallel configuration, whereas it reduces the chaotic behaviour in the perpendicular configuration. Therefore, unlike in the string frame case, the magnetic field introduces a manifest anisotropy in the chaotic behaviour of the string in the Einstein frame. This observation also differentiates the role of chemical potential from that of the magnetic field. Nonetheless, the increase/decrease of chaos with the magnetic field correlates with the tip of the string moving towards/away from the horizon for parallel/perpendicular configuration. It again confirms that the horizon is the source of the chaos. The latter result can be further advocated by the lack of chaos in the stable string dynamics, which is relatively far away from the horizon.

C. Lyapunov exponents

To conclude, we also analyse the Lyapunov exponents in the four-dimension phase space $(\tilde{c}_0, \tilde{c}_1)$. Here, we focus on the system with fixed length $L = 0.75$ and energy $E = 10^{-5}$ for the string's x_1 and x_3 orientations. Like for the string frame calculations, we have taken 8×10^5 time steps with step size 0.001. The numerical results for the convergence of the Lyapunov exponents and their sum are illustrated in Fig. 14. The maximum Lyapunov exponent is recorded in Fig. 15 for x_1 and x_3 string configurations. As in the string frame, our convergence is similar to that of the damped oscillator. The total sum of the Lyapunov

μ	K_1 ()	K_2 ()	K_3 ()	K_4 ()	K_5 ()	K_1 (\perp)	K_2 (\perp)	K_3 (\perp)	K_4 (\perp)	K_5 (\perp)
B = 0.0										
0.0	19.199	33.873	13.720	3.783	7.566	19.199	33.873	13.720	3.783	7.566
0.3	18.728	33.420	13.724	3.808	7.616	18.728	33.420	13.724	3.808	7.616
0.6	17.357	32.062	13.733	3.883	7.766	17.357	32.062	13.733	3.883	7.766
0.9	15.104	29.719	13.696	4.002	8.005	15.104	29.719	13.696	4.002	8.005
1.2	12.220	26.420	13.647	4.184	8.368	12.220	26.420	13.647	4.184	8.368
B = 0.1										
0.0	19.093	33.764	13.725	3.790	7.580	18.904	33.615	13.603	3.768	7.535
0.3	18.628	33.311	13.728	3.815	7.629	18.440	33.168	13.604	3.791	7.583
0.6	17.270	31.955	13.736	3.889	7.779	17.093	31.821	13.610	3.865	7.729
0.9	15.042	29.629	13.700	4.008	8.017	14.914	29.530	13.592	3.986	7.972
1.2	12.188	26.355	13.652	4.189	8.379	12.076	26.279	13.536	4.162	8.323
B = 0.2										
0.0	18.784	33.423	13.740	3.812	7.624	18.076	32.875	13.271	3.725	7.449
0.3	18.636	33.263	13.772	3.830	7.659	17.633	32.444	13.270	3.746	7.492
0.6	17.004	31.640	13.742	3.908	7.815	16.354	31.142	13.267	3.813	7.626
0.9	14.852	29.364	13.711	4.026	8.052	14.345	28.975	13.262	3.931	7.862
1.2	12.091	26.154	13.671	4.207	8.413	11.671	25.877	13.226	4.101	8.201
B = 0.3										
0.0	18.283	32.860	13.767	3.848	7.697	16.770	31.704	12.739	3.652	7.305
0.3	17.855	32.433	13.769	3.872	7.744	16.379	31.306	12.742	3.673	7.346
0.6	16.576	31.117	13.754	3.939	7.878	15.244	30.116	12.750	3.737	7.474
0.9	14.543	28.918	13.730	4.056	8.113	13.400	28.089	12.738	3.841	7.682
1.2	11.929	25.811	13.704	4.236	8.472	10.995	25.229	12.703	3.993	7.986
B = 0.4										
0.0	17.159	31.632	13.782	3.918	7.836	15.091	30.197	12.032	3.551	7.102
0.3	17.218	31.664	13.789	3.918	7.835	14.762	29.838	12.035	3.569	7.139
0.6	15.980	30.378	13.773	3.984	7.968	13.783	28.765	12.045	3.625	7.251
0.9	14.110	28.283	13.762	4.101	8.202	12.191	26.956	12.036	3.716	7.431
1.2	11.689	25.317	13.749	4.278	8.557	10.115	24.408	12.016	3.848	7.697
B = 0.5										
0.0	16.669	30.990	13.808	3.958	7.917	13.161	28.490	11.170	3.419	6.837
0.3	16.305	30.603	13.808	3.980	7.960	12.885	28.183	11.171	3.433	6.867
0.6	15.250	29.425	13.806	4.046	8.091	12.072	27.253	11.174	3.478	6.956
0.9	13.569	27.455	13.810	4.162	8.323	10.777	25.703	11.180	3.555	7.110
1.2	11.334	24.636	13.774	4.325	8.650	9.080	23.524	11.183	3.668	7.336

TABLE VII. K values for various chemical potentials μ and magnetic field strengths B for both parallel and perpendicular string orientations in the Einstein frame. The string length is set to $L = 0.75$. All quantities are expressed in units of GeV.

exponents converges to zero, suggesting that the system remains conservative. This result is true for all magnetic field and chemical potential values, irrespective of the relative orientation of the string and magnetic field.

From the Poincaré plots (Fig. 13), we already observe that the scatter points were concentrated near the origin of the phase space. This observation suggests the dynamics of the string becomes more chaotic as its tip approaches the horizon. This result is now also supported by the largest Lyapunov exponents λ_{max} for both parallel and perpendicular string orientation, as shown in figure 15.

The maximal Lyapunov exponent is extracted for all magnetic field and chemical potential values; the data is then plotted for the x_1 and x_3 string orientation cases with the string length fixed. In contrast to the string frame case, we see that λ_{max} increases

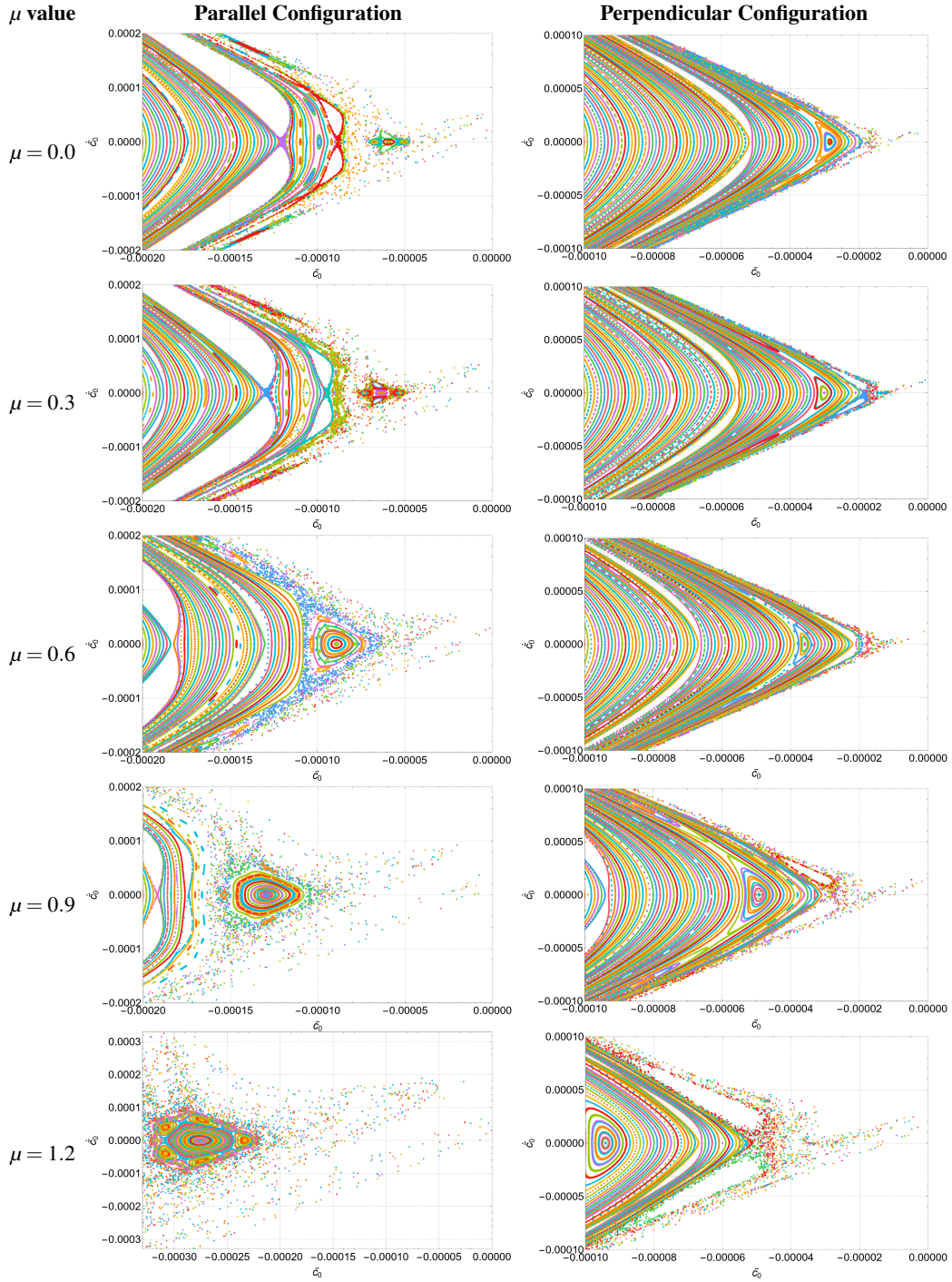


FIG. 13. The Poincaré sections for different values of μ . The left panel is for x_1 orientation (parallel), while the right panel is for x_3 orientation (perpendicular). The section is identified by $\tilde{c}_1(t) = 0$ and $\tilde{c}_1(t) \geq 0$ with $E = 10^{-5}$. The string length is fixed at $L = 0.75$ and the magnetic field is set to $B = 0.2$. All values in GeV units.

as μ increases for both x_1 and x_3 string configurations when B is small, i.e., the overall system exhibits an enhanced chaotic nature as μ increases, irrespective of its orientation relative to the magnetic field. If we look more closely, there is actually a difference in the behaviour of λ_{max} between the x_1 and x_3 string orientations for large B values. Indeed, in the case of the x_1 orientation, increasing the μ value significantly increases λ_{max} while it remains almost constant for the x_3 orientation. This highlights one important aspect of the interplay of the magnetic field with the chemical potential. Since increasing the B value increases the chaos in the x_1 orientation and decreases it in the x_3 orientation, the effect of increasing the chemical potential also differs in both orientations.

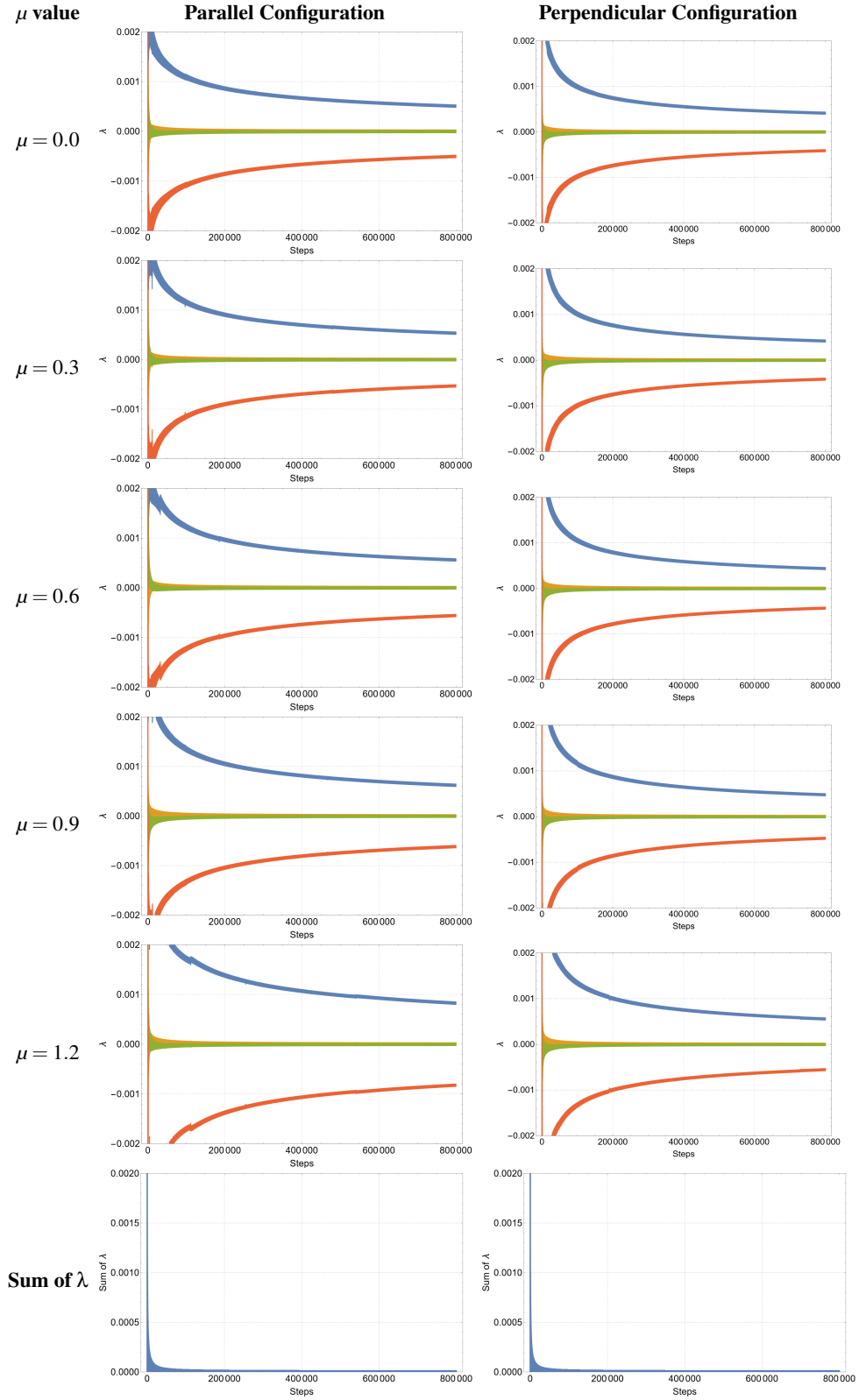


FIG. 14. Convergence plots of the four Lyapunov exponents for different values of μ for a string oriented parallel (left column) and perpendicular (right column) to the magnetic field. Here the initial conditions $(\tilde{c}_0, \dot{\tilde{c}}_0, \tilde{c}_1) = (-0.002, 0, 0.001)$ are taken and fixed $L = 0.75$, $E = 10^{-5}$, and $B = 0.2$ are used. The sum of the Lyapunov exponents is displayed in the bottom row for $\mu = 0.6$ and $B = 0.2$. Similar converging behaviour is observed for all values of the magnetic field and chemical potential. All quantities are expressed in units of GeV.

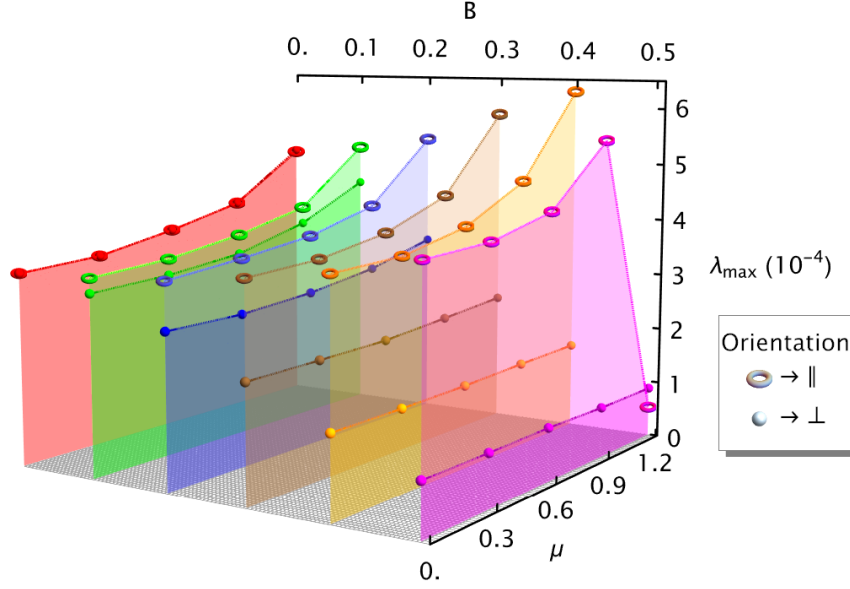


FIG. 15. Comparison of the maximum Lyapunov exponent λ_{\max} for the x_1 (parallel) and x_3 (perpendicular) magnetic field orientations for various values of B and μ near the unstable saddle point. Data points are colour-coded as follows: red for $B = 0.0$, green for $B = 0.1$, blue for $B = 0.2$, brown for $B = 0.3$, orange for $B = 0.4$, and magenta for $B = 0.5$. Here, we use the initial conditions $(\tilde{c}_0, \tilde{c}_0, \tilde{c}_1) = (-0.002, 0, 0.001)$. The string length is fixed at $L = 0.75$ and $E = 10^{-5}$.

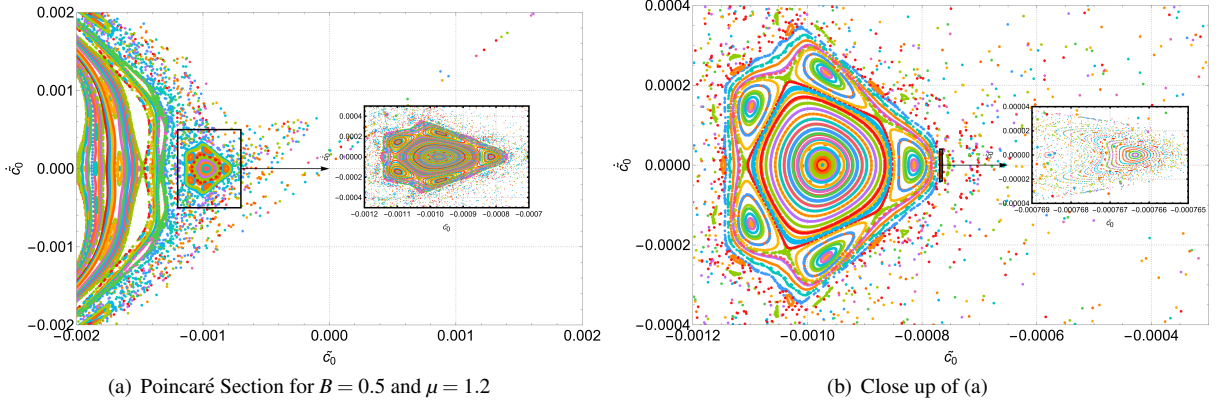


FIG. 16. Poincaré section, identified by $\tilde{c}_1(t) = 0$ and $\dot{\tilde{c}}_1(t) \geq 0$ with $E = 10^{-5}$, for $\mu = 1.2$ with the magnetic field fixed at $B = 0.5$. The section reveals a fractal island near the origin, with the fractal nature further examined in an enlarged view. The string length is fixed at $L = 0.75$.

From Fig. 15, we also see a small departure from the overall behaviour of λ_{\max} in the x_1 configuration. In particular, there is a sudden drop in λ_{\max} for $B = 0.5$ as μ goes from 0.9 to 1.2. This differs from the Lyapunov exponent's overall nature as we increase μ , keeping the B value fixed. The reason for such difference is what appears to be the presence of fractal islands in the vicinity of origin, which are like small non-chaotic pockets in a sea of chaos. This can be explicitly observed in the Poincaré section profile for $\mu = 1.2$, shown in Fig. 16. The occurrence of these islands is related to KAM (Kolmogorov–Arnold–Moser) theory and transition to chaos [146]. The KAM theorem is one of the most important results in the study of dynamical systems. Oversimplifying and under certain assumptions, if a tiny Hamiltonian perturbation is applied to a system, some of the so-called tori—to which the phase space trajectories are confined, indicative of quasi-periodicity—only get slightly deformed, while most do get destroyed. Increasing the chemical potential for a given magnetic field increases the intensity of our perturbations, and most regular orbits are thus destroyed to form “dust”. However, some tori exist that do not get destroyed but only get deformed to form small fractal islands surrounded by chaos. This intriguing result undoubtedly warrants a comprehensive and meticulously detailed investigation in its own right. In any case, in QCD-like gauge theories, interesting features are expected to appear with chemical potential in the range of $\mu \lesssim 1$ GeV. The above non-trivial trend of the Lyapunov exponent that appears for $\mu \gtrsim 1$ GeV in our model thus lies outside the physically interesting range of the chemical potential.

We further find that the choice of the string orientation significantly affects the value of the maximum Lyapunov exponent λ_{max} . While the chemical potential enhances the chaotic nature of the string, this effect is more significant in the parallel configuration. This suggests that the anisotropic nature of the system dynamics depends on its orientation with the magnetic field. We further find that λ_{max} increases/decreases with the magnetic field for parallel/perpendicular orientation of the string. Our Lyapunov exponent analysis, therefore, further confirms our previous expectation that the magnetic field induces anisotropy in the string dynamics, i.e., the chaos in the string dynamics increases/decreases with the magnetic field in parallel/perpendicular directions. This observation also makes it clear that the effect of chemical potential is dissimilar to that of the magnetic field regarding the string dynamics.

D. Saddle point analysis and the MSS bound

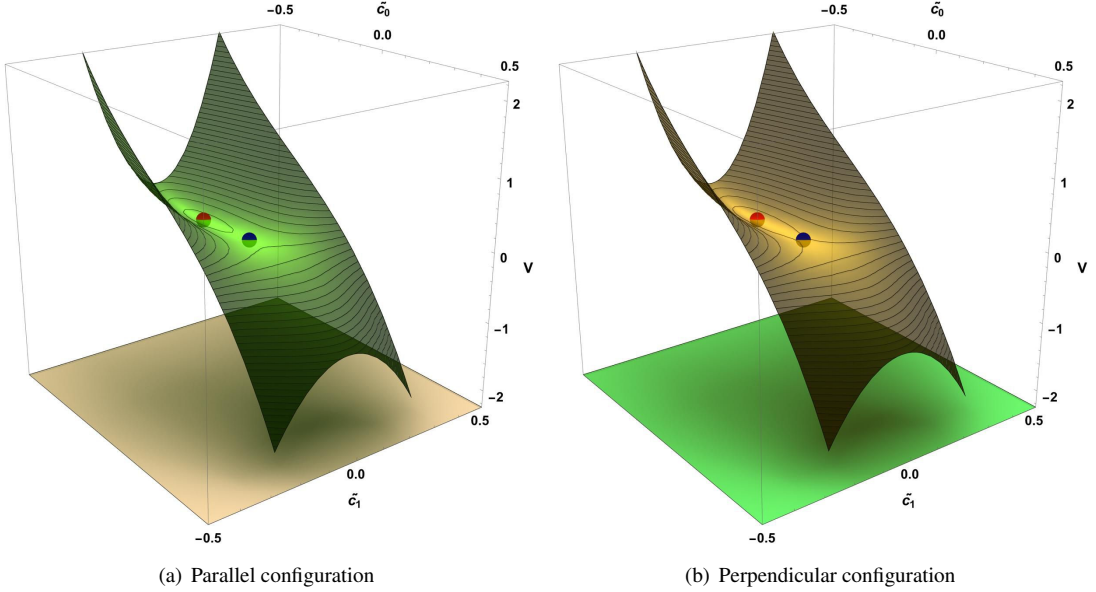


FIG. 17. Three-dimensional plot of the potential. The red dot corresponds to the local minima and the blue dot corresponds to the saddle point. Here $B = 0.2$, $\mu = 0.6$, and $L = 0.75$ are used. In units of GeV.

To complete our analysis, we have again checked the validity of the MSS bound in the Einstein frame. As mentioned earlier, the perturbation around the string also generates a trapping potential, shown in Fig. 17, with stable and unstable fixed points in the Einstein frame. We find that λ_{max} inside the potential trap is around three orders of magnitude smaller than the MSS bound for all chemical potential and magnetic field values, thereby satisfying the MSS bound. Similarly, like in the string frame case, the Lyapunov exponents at the unstable fixed point again asymptotically converge to $(\sqrt{-\omega_0^2}, -\sqrt{-\omega_0^2}, 0, 0)$. The values of ω_0^2 are given in Table VI. This gives us the largest Lyapunov exponent at the saddle point $\lambda_{max} = \sqrt{-\omega_0^2}$. Although λ_{max} at the unstable fixed point is three orders of magnitude higher than the stable point, it still remains below the MSS bound. This is explicitly shown in Fig. 18. Moreover, λ_{max} at the unstable fixed point is found to be decreasing with μ and B for both orientations of the string. The chemical potential weakens the dependence of the system dynamics to the initial conditions, increasing with μ but also increasing/decreasing for parallel/perpendicular magnetic fields. This is another result different from the string frame case, where λ_{max} exhibited similar behaviour near the unstable and stable fixed points for the string's parallel and perpendicular orientation. Our analysis, therefore, provides a curious and intriguing example where the Lyapunov exponent exhibits a different structure depending upon the fixed points involved in the system.

V. CONCLUSION

In this paper, we have numerically analyzed the effects of chemical potential and magnetic field on the dynamics of the confining string based on the EMD model of [86, 91] that includes two $U(1)$ gauge fields to incorporate both chemical potential and background magnetic field in the dual boundary QCD system. The model has been shown elsewhere to capture several

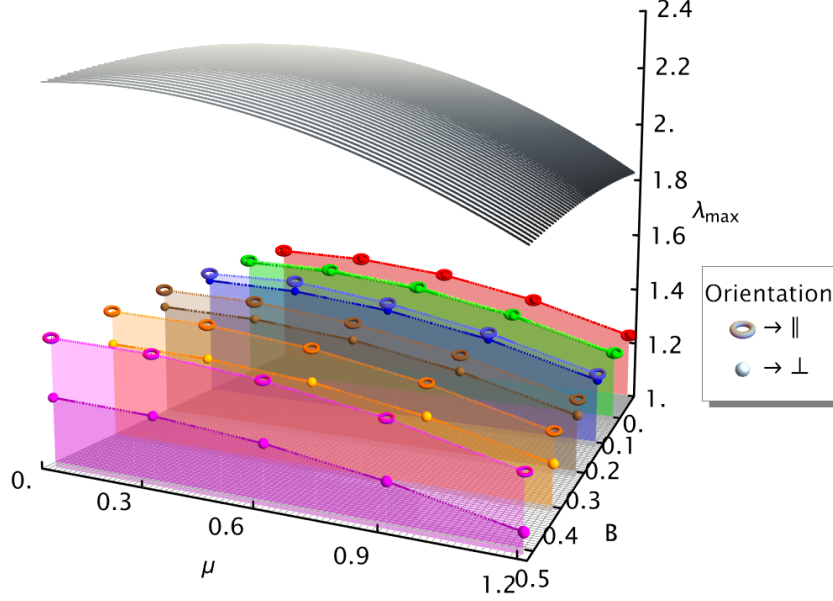


FIG. 18. Comparison of the maximum Lyapunov exponent λ_{max} and the MSS bound for x_1 (\parallel) and x_3 (\perp) orientations for different B and μ values at the unstable saddle point. Here red, green, blue, brown, orange, and magenta data points correspond to $B = 0.0, 0.1, 0.2, 0.3, 0.4,$ and 0.5 , respectively. The MSS bound is shown by the grey surface above the data points.

lattice-supported QCD features. Here, we analysed the system in both the string and Einstein frames. Our investigations reveal that the effects strongly depend on the considered gravitational frame.

To be more precise, in the string frame we find that, as we increase the chemical potential the tip of the string moves away from the horizon both in parallel and perpendicular directions of the magnetic field. Similar behaviour is also observed with increasing magnetic field in both directions. The Poincaré section exhibits a more structured picture with a decrease in the number of scatter points as the value of the chemical potential and magnetic field increases. This behaviour is common for both magnetic field directions. The largest Lyapunov exponent decreases as we increase the value of the chemical potential and magnetic field, also irrespective of the orientation of the magnetic field. The Lyapunov exponent is, however, smaller in the perpendicular direction when compared to the parallel one. The largest Lyapunov exponent always remains below the MSS upper bound both at the stable and unstable fixed points. These results confirm the role of chemical potential and magnetic field as stabilisers of the system, with a stronger stabilisation in the perpendicular direction. Chaos only shows up for the unstable string configuration, which is near the horizon, whereas no chaos appears in the stable string configuration, which is relatively far away from the horizon, highlighting the horizon as the source of the chaos.

On the other hand, in the Einstein frame, as we increase the chemical potential the tip of the string moves towards the horizon both in parallel and perpendicular directions of the magnetic field. With increasing magnetic field, the tip of the string moves towards/away from the horizon for the parallel/perpendicular directions. The Poincaré section becomes less structured around the origin as we increase the chemical potential. In fact, the Poincaré section becomes less/more structured when the magnetic field is increased in the parallel/perpendicular direction. The largest Lyapunov exponent increases as we increase the chemical potential irrespective of the orientation of the magnetic field. Similarly, the largest Lyapunov exponent increases/decreases with the magnetic field for parallel/perpendicular cases. These results are quite different from the string frame case. From the Poincaré section and the Lyapunov exponents, we conclude that the effect of the chemical potential is to destabilise the system as it increases (as it is evident from Figure 15). The largest Lyapunov exponent again always remains below the MSS bound both at the stable and unstable fixed points. Interestingly, as opposed to the string frame case, the largest Lyapunov exponent exhibits distinct chemical potential and magnetic field-related behaviour near the unstable and stable fixed points for both parallel and perpendicular orientations.

In summary, our results clearly distinguish between the string and Einstein frames, also in the context of holographic QCD. The choice of frame considerably alters the dynamical nature of the system. Specifically, in the string frame, the dependence of the confined quark-antiquark pair's dynamics on the initial conditions is shown to weaken as the chemical potential increases. Conversely, in the Einstein frame, the dynamics of the quark-antiquark pair were found to become more sensitive to its initial conditions with increasing chemical potential. These contrasting results underscore the importance of frame selection in theoretical predictions and interpretations thereof within holographic QCD. Which one is preferred can only be confirmed from further studies, including those from other non-perturbative QCD approaches.

ACKNOWLEDGEMENTS

The work of S.M. is supported by the core research grant from the Science and Engineering Research Board, a statutory body under the Department of Science and Technology, Government of India, under grant agreement number CRG/2023/007670.

-
- [1] R. Pullirsch, K. Rabitsch, T. Wettig and H. Markum, *Evidence for quantum chaos in the plasma phase of QCD*, *Phys. Lett. B* **427** (1998) 119 [hep-ph/9803285].
- [2] Y. Asano, D. Kawai, H. Kyono and K. Yoshida, *Chaotic strings in a near Penrose limit of $AdS_5 \times T^{1,1}$* , *JHEP* **08** (2015) 060 [1505.07583].
- [3] R. Pullirsch, H. Markum, K. Rabitsch and T. Wettig, *Quantum chaos and QCD at finite chemical potential*, *Nucl. Phys. B Proc. Suppl.* **73** (1999) 486 [hep-lat/9809057].
- [4] E. Bittner, H. Markum and R. Pullirsch, *Quantum chaos and chiral symmetry at the QCD and QED phase transition*, *Nucl. Phys. B Proc. Suppl.* **96** (2001) 189 [hep-lat/0009002].
- [5] K. Hashimoto, K. Murata and K. Yoshida, *Chaos in chiral condensates in gauge theories*, *Phys. Rev. Lett.* **117** (2016) 231602 [1605.08124].
- [6] D.S. Ageev, *Chaotic nature of holographic QCD*, *Phys. Rev. D* **104** (2021) 126013 [2105.04589].
- [7] G. Yadav, S.S. Kushwah and A. Misra, *Pole-skipping and chaos in hot M QCD*, *JHEP* **05** (2024) 015 [2311.09306].
- [8] N. Losacco, *Holographic Study of the $Q\bar{Q}$ Chaotic Dynamics in General Thermal Background*, *EPJ Web Conf.* **270** (2022) 00025 [2211.16840].
- [9] B. Müller and A. Trayanov, *Deterministic chaos in non-Abelian lattice gauge theory*, *Phys. Rev. Lett.* **68** (1992) 3387.
- [10] T.S. Biró, C. Gong and B. Müller, *Lyapunov exponent and plasmon damping rate in non-abelian gauge theories*, *Phys. Rev. D* **52** (1995) 1260.
- [11] H. Tsukiji, H. Iida, T. Kunihiro, A. Ohnishi and T.T. Takahashi, *Entropy production from chaoticity in Yang-Mills field theory with use of the Husimi function*, *Phys. Rev. D* **94** (2016) 091502 [1603.04622].
- [12] T. Kunihiro, B. Muller, A. Ohnishi, A. Schafer, T.T. Takahashi and A. Yamamoto, *Chaotic behavior in classical Yang-Mills dynamics*, *Phys. Rev. D* **82** (2010) 114015 [1008.1156].
- [13] J.M. Maldacena, *The Large N limit of superconformal field theories and supergravity*, *Adv. Theor. Math. Phys.* **2** (1998) 231 [hep-th/9711200].
- [14] E. Witten, *Anti-de Sitter space and holography*, *Adv. Theor. Math. Phys.* **2** (1998) 253 [hep-th/9802150].
- [15] S.S. Gubser, I.R. Klebanov and A.M. Polyakov, *Gauge theory correlators from noncritical string theory*, *Phys. Lett. B* **428** (1998) 105 [hep-th/9802109].
- [16] L.A. Pando Zayas and C.A. Terrero-Escalante, *Chaos in the Gauge / Gravity Correspondence*, *JHEP* **09** (2010) 094 [1007.0277].
- [17] M. Blake and R.A. Davison, *Chaos and pole-skipping in rotating black holes*, *JHEP* **01** (2022) 013 [2111.11093].
- [18] S. Giombi, S. Komatsu and B. Offertaler, *Chaos and the reparametrization mode on the AdS_2 string*, *JHEP* **09** (2023) 023 [2212.14842].
- [19] P. Basu, D. Das and A. Ghosh, *Integrability Lost*, *Phys. Lett. B* **699** (2011) 388 [1103.4101].
- [20] P. Basu and L.A. Pando Zayas, *Chaos rules out integrability of strings on $AdS_5 \times T^{1,1}$* , *Phys. Lett. B* **700** (2011) 243 [1103.4107].
- [21] A. Stepanchuk and A.A. Tseytlin, *On (non)integrability of classical strings in p-brane backgrounds*, *J. Phys. A* **46** (2013) 125401 [1211.3727].
- [22] D. Giataganas, L.A. Pando Zayas and K. Zoubos, *On Marginal Deformations and Non-Integrability*, *JHEP* **01** (2014) 129 [1311.3241].
- [23] X. Bai, B.-H. Lee, T. Moon and J. Chen, *Chaos in Lifshitz Spacetimes*, *J. Korean Phys. Soc.* **68** (2016) 639 [1406.5816].
- [24] K.L. Panigrahi and M. Samal, *Chaos in classical string dynamics in $\hat{\gamma}$ deformed $AdS_5 \times T^{1,1}$* , *Phys. Lett. B* **761** (2016) 475 [1605.05638].
- [25] P. Basu, P. Chaturvedi and P. Samantray, *Chaotic dynamics of strings in charged black hole backgrounds*, *Phys. Rev. D* **95** (2017) 066014 [1607.04466].
- [26] Y. Asano, H. Kyono and K. Yoshida, *Melnikov's method in String Theory*, *JHEP* **09** (2016) 103 [1607.07302].
- [27] T. Ishii, K. Murata and K. Yoshida, *Fate of chaotic strings in a confining geometry*, *Phys. Rev. D* **95** (2017) 066019 [1610.05833].
- [28] K.S. Rigatos, *Nonintegrability of $L^{a,b,c}$ quiver gauge theories*, *Phys. Rev. D* **102** (2020) 106022 [2009.11878].
- [29] J. Pal, *Chaotic string dynamics in bosonic η -deformed $AdS_5 \times T^{1,1}$ background*, *Mod. Phys. Lett. A* **38** (2023) 2350142 [2304.10474].
- [30] J.M. Penín and K.C. Rigatos, *Evidence for a four-dimensional $N=1$ integrable quiver in massive type IIA supergravity*, *Phys. Rev. D* **109** (2024) 126007.
- [31] B. Shukla, O. Riyaz and S. Mahapatra, *Classical and quantum chaos of closed strings on a charged confining holographic background*, 2411.12536.
- [32] B. Shukla, D. Dudal and S. Mahapatra, *Anisotropic and frame dependent chaos of suspended strings from a dynamical holographic QCD model with magnetic field*, *JHEP* **06** (2023) 178 [2303.15716].
- [33] K. Hashimoto, K. Murata and N. Tanahashi, *Chaos of Wilson Loop from String Motion near Black Hole Horizon*, *Phys. Rev. D* **98** (2018) 086007 [1803.06756].
- [34] P. Colangelo, F. De Fazio and N. Losacco, *Chaos in a $Q\bar{Q}$ system at finite temperature and baryon density*, *Phys. Rev. D* **102** (2020) 074016 [2007.06980].

- [35] T. Akutagawa, K. Hashimoto, K. Murata and T. Ota, *Chaos of QCD string from holography*, *Phys. Rev. D* **100** (2019) 046009 [1903.04718].
- [36] P. Colangelo, F. Giannuzzi and N. Losacco, *Chaotic dynamics of a suspended string in a gravitational background with magnetic field*, *Phys. Lett. B* **827** (2022) 136949 [2111.09441].
- [37] D. Giataganas and K. Zoubos, *Non-integrability and Chaos with Unquenched Flavor*, *JHEP* **10** (2017) 042 [1707.04033].
- [38] M. Blake, H. Lee and H. Liu, *A quantum hydrodynamical description for scrambling and many-body chaos*, *JHEP* **10** (2018) 127 [1801.00010].
- [39] M. Blake, R.A. Davison, S. Grozdanov and H. Liu, *Many-body chaos and energy dynamics in holography*, *JHEP* **10** (2018) 035 [1809.01169].
- [40] S. Grozdanov, *On the connection between hydrodynamics and quantum chaos in holographic theories with stringy corrections*, *JHEP* **01** (2019) 048 [1811.09641].
- [41] E.B. Rozenbaum, S. Ganeshan and V. Galitski, *Lyapunov Exponent and Out-of-Time-Ordered Correlator's Growth Rate in a Chaotic System*, *Phys. Rev. Lett.* **118** (2017) 086801 [1609.01707].
- [42] K. Hashimoto, K. Murata and R. Yoshii, *Out-of-time-order correlators in quantum mechanics*, *JHEP* **10** (2017) 138 [1703.09435].
- [43] I. García-Mata, M. Saraceno, R.A. Jalabert, A.J. Roncaglia and D.A. Wisniacki, *Chaos signatures in the short and long time behavior of the out-of-time ordered correlator*, *Phys. Rev. Lett.* **121** (2018) 210601 [1806.04281].
- [44] B. Kobrin, Z. Yang, G.D. Kahanamoku-Meyer, C.T. Olund, J.E. Moore, D. Stanford et al., *Many-Body Chaos in the Sachdev-Ye-Kitaev Model*, *Phys. Rev. Lett.* **126** (2021) 030602 [2002.05725].
- [45] K. Hashimoto, K.-B. Huh, K.-Y. Kim and R. Watanabe, *Exponential growth of out-of-time-order correlator without chaos: inverted harmonic oscillator*, *JHEP* **11** (2020) 068 [2007.04746].
- [46] M. Mezei and G. Sárosi, *Chaos in the butterfly cone*, *JHEP* **01** (2020) 186 [1908.03574].
- [47] P. Caputa, J.M. Magan and D. Patramanis, *Geometry of Krylov complexity*, *Phys. Rev. Res.* **4** (2022) 013041 [2109.03824].
- [48] B. Bhattacharjee, X. Cao, P. Nandy and T. Pathak, *Krylov complexity in saddle-dominated scrambling*, *JHEP* **05** (2022) 174 [2203.03534].
- [49] E. Rabinovici, A. Sánchez-Garrido, R. Shir and J. Sonner, *Krylov complexity from integrability to chaos*, *JHEP* **07** (2022) 151 [2207.07701].
- [50] A. Avdoshkin, A. Dymarsky and M. Smolkin, *Krylov complexity in quantum field theory, and beyond*, 2212.14429.
- [51] K. Hashimoto, K. Murata, N. Tanahashi and R. Watanabe, *Krylov complexity and chaos in quantum mechanics*, *JHEP* **11** (2023) 040 [2305.16669].
- [52] V. Balasubramanian, J.M. Magan and Q. Wu, *Quantum chaos, integrability, and late times in the Krylov basis*, 2312.03848.
- [53] J.S. Cotler, G. Gur-Ari, M. Hanada, J. Polchinski, P. Saad, S.H. Shenker et al., *Black Holes and Random Matrices*, *JHEP* **05** (2017) 118 [1611.04650].
- [54] P. Hayden, S. Nezami, X.-L. Qi, N. Thomas, M. Walter and Z. Yang, *Holographic duality from random tensor networks*, *JHEP* **11** (2016) 009 [1601.01694].
- [55] A. Kar, L. Lamprou, M. Rozali and J. Sully, *Random matrix theory for complexity growth and black hole interiors*, *JHEP* **01** (2022) 016 [2106.02046].
- [56] A. Altland, D. Bagrets, P. Nayak, J. Sonner and M. Vielma, *From operator statistics to wormholes*, *Phys. Rev. Res.* **3** (2021) 033259 [2105.12129].
- [57] V. Balasubramanian, M. Berkooz, S.F. Ross and J. Simon, *Black Holes, Entanglement and Random Matrices*, *Class. Quant. Grav.* **31** (2014) 185009 [1404.6198].
- [58] L.A. Pando Zayas and D. Reichmann, *A String Theory Explanation for Quantum Chaos in the Hadronic Spectrum*, *JHEP* **04** (2013) 083 [1209.5902].
- [59] V. Jahnke, *Recent developments in the holographic description of quantum chaos*, *Adv. High Energy Phys.* **2019** (2019) 9632708 [1811.06949].
- [60] A.M. Lyapunov, *The general problem of the stability of motion*, *International Journal of Control* **55** (1992) 531.
- [61] X. Guo, Y. Lu, B. Mu and P. Wang, *Probing phase structure of black holes with Lyapunov exponents*, *JHEP* **08** (2022) 153 [2205.02122].
- [62] S. Yang, J. Tao, B. Mu and A. He, *Lyapunov exponents and phase transitions of Born-Infeld AdS black holes*, *JCAP* **07** (2023) 045 [2304.01877].
- [63] X. Lyu, J. Tao and P. Wang, *Probing the thermodynamics of charged Gauss Bonnet AdS black holes with the Lyapunov exponent*, *Eur. Phys. J. C* **84** (2024) 974 [2312.11912].
- [64] A.N. Kumara, S. Punacha and M.S. Ali, *Lyapunov exponents and phase structure of Lifshitz and hyperscaling violating black holes*, *JCAP* **07** (2024) 061 [2401.05181].
- [65] Y.-Z. Du, H.-F. Li, Y.-B. Ma and Q. Gu, *Phase structure of the de Sitter Spacetime with KR field based on the Lyapunov exponent*, 2403.20083.
- [66] N.J. Gogoi, S. Acharjee and P. Phukon, *Lyapunov exponents and phase transition of Hayward AdS black hole*, *Eur. Phys. J. C* **84** (2024) 1144 [2404.03947].
- [67] B. Shukla, P.P. Das, D. Dudal and S. Mahapatra, *Interplay between the Lyapunov exponents and phase transitions of charged AdS black holes*, *Phys. Rev. D* **110** (2024) 024068 [2404.02095].
- [68] J. Maldacena, S.H. Shenker and D. Stanford, *A bound on chaos*, *JHEP* **08** (2016) 106 [1503.01409].
- [69] S.D. Avramis, K. Sfetsos and K. Siampos, *Stability of strings dual to flux tubes between static quarks in $N = 4$ SYM*, *Nucl. Phys. B* **769** (2007) 44 [hep-th/0612139].
- [70] R.E. Arias and G.A. Silva, *Wilson loops stability in the gauge/string correspondence*, *JHEP* **01** (2010) 023 [0911.0662].

- [71] C. Nunez, M. Piai and A. Rago, *Wilson Loops in string duals of Walking and Flavored Systems*, *Phys. Rev. D* **81** (2010) 086001 [0909.0748].
- [72] L. Bellantuono, P. Colangelo, F. De Fazio, F. Giannuzzi and S. Nicotri, *Quarkonium dissociation in a far-from-equilibrium holographic setup*, *Phys. Rev. D* **96** (2017) 034031 [1706.04809].
- [73] V. Skokov, A.Y. Illarionov and V. Toneev, *Estimate of the magnetic field strength in heavy-ion collisions*, *Int. J. Mod. Phys. A* **24** (2009) 5925 [0907.1396].
- [74] A. Bzdak and V. Skokov, *Event-by-event fluctuations of magnetic and electric fields in heavy ion collisions*, *Phys. Lett. B* **710** (2012) 171 [1111.1949].
- [75] M. D'Elia, S. Mukherjee and F. Sanfilippo, *QCD Phase Transition in a Strong Magnetic Background*, *Phys. Rev. D* **82** (2010) 051501 [1005.5365].
- [76] W.-T. Deng and X.-G. Huang, *Event-by-event generation of electromagnetic fields in heavy-ion collisions*, *Phys. Rev. C* **85** (2012) 044907 [1201.5108].
- [77] K. Tuchin, *Particle production in strong electromagnetic fields in relativistic heavy-ion collisions*, *Adv. High Energy Phys.* **2013** (2013) 490495 [1301.0099].
- [78] V. Voronyuk, V.D. Toneev, W. Cassing, E.L. Bratkovskaya, V.P. Konchakovski and S.A. Voloshin, *(Electro-)Magnetic field evolution in relativistic heavy-ion collisions*, *Phys. Rev. C* **83** (2011) 054911 [1103.4239].
- [79] S.S. Gubser and A. Nellore, *Mimicking the QCD equation of state with a dual black hole*, *Phys. Rev. D* **78** (2008) 086007 [0804.0434].
- [80] U. Gursoy and E. Kiritsis, *Exploring improved holographic theories for QCD: Part I*, *JHEP* **02** (2008) 032 [0707.1324].
- [81] U. Gursoy, E. Kiritsis, L. Mazzanti, G. Michalogiorgakis and F. Nitti, *Improved Holographic QCD*, *Lect. Notes Phys.* **828** (2011) 79 [1006.5461].
- [82] O. DeWolfe, S.S. Gubser and C. Rosen, *A holographic critical point*, *Phys. Rev. D* **83** (2011) 086005 [1012.1864].
- [83] D. Dudal and S. Mahapatra, *Thermal entropy of a quark-antiquark pair above and below deconfinement from a dynamical holographic QCD model*, *Phys. Rev. D* **96** (2017) 126010 [1708.06995].
- [84] R.-G. Cai, S. He and D. Li, *A hQCD model and its phase diagram in Einstein-Maxwell-Dilaton system*, *JHEP* **03** (2012) 033 [1201.0820].
- [85] S. He, S.-Y. Wu, Y. Yang and P.-H. Yuan, *Phase Structure in a Dynamical Soft-Wall Holographic QCD Model*, *JHEP* **04** (2013) 093 [1301.0385].
- [86] H. Bohra, D. Dudal, A. Hajilou and S. Mahapatra, *Chiral transition in the probe approximation from an Einstein-Maxwell-dilaton gravity model*, *Phys. Rev. D* **103** (2021) 086021 [2010.04578].
- [87] D. Dudal, A. Hajilou and S. Mahapatra, *A quenched 2-flavour Einstein–Maxwell–Dilaton gauge-gravity model*, *Eur. Phys. J. A* **57** (2021) 142 [2103.01185].
- [88] R. Rougemont, R. Critelli and J. Noronha, *Holographic calculation of the QCD crossover temperature in a magnetic field*, *Phys. Rev. D* **93** (2016) 045013 [1505.07894].
- [89] S.I. Finazzo, R. Critelli, R. Rougemont and J. Noronha, *Momentum transport in strongly coupled anisotropic plasmas in the presence of strong magnetic fields*, *Phys. Rev. D* **94** (2016) 054020 [1605.06061].
- [90] I.Y. Aref'eva, A. Hajilou, A. Nikolaev and P. Slepov, *Holographic QCD running coupling for light quarks in strong magnetic field*, *Phys. Rev. D* **110** (2024) 086021 [2407.11924].
- [91] H. Bohra, D. Dudal, A. Hajilou and S. Mahapatra, *Anisotropic string tensions and inversely magnetic catalyzed deconfinement from a dynamical AdS/QCD model*, *Phys. Lett. B* **801** (2020) 135184 [1907.01852].
- [92] U. Gursoy, M. Jarvinen and G. Nijs, *Holographic QCD in the Veneziano Limit at a Finite Magnetic Field and Chemical Potential*, *Phys. Rev. Lett.* **120** (2018) 242002 [1707.00872].
- [93] I.Y. Aref'eva, K. Rannu and P. Slepov, *Holographic model for heavy quarks in anisotropic hot dense QGP with external magnetic field*, *JHEP* **07** (2021) 161 [2011.07023].
- [94] I.Y. Aref'eva, K. Rannu and P. Slepov, *Einstein-dilaton-four-Maxwell Holographic Anisotropic Models*, 2409.12131.
- [95] D. Dudal and S. Mahapatra, *Interplay between the holographic QCD phase diagram and entanglement entropy*, *JHEP* **07** (2018) 120 [1805.02938].
- [96] S. Mahapatra, *Interplay between the holographic QCD phase diagram and mutual \mathcal{N} & n -partite information*, *JHEP* **04** (2019) 137 [1903.05927].
- [97] D. Dudal and S. Mahapatra, *Confining gauge theories and holographic entanglement entropy with a magnetic field*, *JHEP* **04** (2017) 031 [1612.06248].
- [98] R. Rougemont, R. Critelli and J. Noronha, *Anisotropic heavy quark potential in strongly-coupled $\mathcal{N} = 4$ SYM in a magnetic field*, *Phys. Rev. D* **91** (2015) 066001 [1409.0556].
- [99] J.F. Fuini and L.G. Yaffe, *Far-from-equilibrium dynamics of a strongly coupled non-Abelian plasma with non-zero charge density or external magnetic field*, *JHEP* **07** (2015) 116 [1503.07148].
- [100] C. Cartwright and M. Kaminski, *Correlations far from equilibrium in charged strongly coupled fluids subjected to a strong magnetic field*, *JHEP* **09** (2019) 072 [1904.11507].
- [101] K. Fukushima and A. Okutsu, *Electric conductivity with the magnetic field and the chiral anomaly in a holographic QCD model*, *Phys. Rev. D* **105** (2022) 054016 [2106.07968].
- [102] A. Ballon-Bayona, J.P. Shock and D. Zoakos, *Magnetising the $\mathcal{N} = 4$ Super Yang-Mills plasma*, *JHEP* **06** (2022) 154 [2203.00050].
- [103] D.M. Rodrigues, E. Folco Capossoli and H. Boschi-Filho, *Deconfinement phase transition in a magnetic field in $2 + 1$ dimensions from holographic models*, *Phys. Lett. B* **780** (2018) 37 [1709.09258].
- [104] I.Y. Aref'eva, A. Hajilou, K. Rannu and P. Slepov, *Magnetic catalysis in holographic model with two types of anisotropy for heavy quarks*, *Eur. Phys. J. C* **83** (2023) 1143 [2305.06345].

- [105] I.Y. Aref'eva, A. Ermakov and P. Slepov, *Direct photons emission rate and electric conductivity in twice anisotropic QGP holographic model with first-order phase transition*, *Eur. Phys. J. C* **82** (2022) 85 [2104.14582].
- [106] S.S. Jena, B. Shukla, D. Dudal and S. Mahapatra, *Entropic force and real-time dynamics of holographic quarkonium in a magnetic field*, *Phys. Rev. D* **105** (2022) 086011 [2202.01486].
- [107] P. Jain, S.S. Jena and S. Mahapatra, *Holographic confining-deconfining gauge theories and entanglement measures with a magnetic field*, *Phys. Rev. D* **107** (2023) 086016 [2209.15355].
- [108] I.Y. Aref'eva, A. Ermakov, K. Rannu and P. Slepov, *Holographic model for light quarks in anisotropic hot dense QGP with external magnetic field*, *Eur. Phys. J. C* **83** (2023) 79 [2203.12539].
- [109] X. Chen, L. Zhang and D. Hou, *Running coupling constant at finite chemical potential and magnetic field from holography **, *Chin. Phys. C* **46** (2022) 073101 [2108.03840].
- [110] N.R.F. Braga and R. da Mata, *Configuration entropy description of charmonium dissociation under the influence of magnetic fields*, *Phys. Lett. B* **811** (2020) 135918 [2008.10457].
- [111] J. Zhou, X. Chen, Y.-Q. Zhao and J. Ping, *Thermodynamics of heavy quarkonium in a magnetic field background*, *Phys. Rev. D* **102** (2020) 086020 [2006.09062].
- [112] A. Ballon-Bayona, J.P. Shock and D. Zoakos, *Magnetic catalysis and the chiral condensate in holographic QCD*, *JHEP* **10** (2020) 193 [2005.00500].
- [113] Y.-Q. Zhao and D. Hou, *Vector meson spectral function in a dynamical AdS/QCD model*, *Eur. Phys. J. C* **82** (2022) 1102 [2108.08479].
- [114] D. Dudal and T.G. Mertens, *Holographic estimate of heavy quark diffusion in a magnetic field*, *Phys. Rev. D* **97** (2018) 054035 [1802.02805].
- [115] S.S. Jena, J. Barman, B. Toniato, D. Dudal and S. Mahapatra, *A dynamical Einstein-Born-Infeld-dilaton model and holographic quarkonium melting in a magnetic field*, 2408.14813.
- [116] A. Ballon-Bayona, S. Bartz, L.A.H. Mamani and D.M. Rodrigues, *The chiral transition and meson melting within improved holographic soft wall models*, 2410.23471.
- [117] N.R.F. Braga, Y.F. Ferreira and L.F. Ferreira, *Configuration entropy and stability of bottomonium radial excitations in a plasma with magnetic fields*, *Phys. Rev. D* **105** (2022) 114044 [2110.04560].
- [118] R. Rougemont, J. Grefa, M. Hippert, J. Noronha, J. Noronha-Hostler, I. Portillo et al., *Hot QCD phase diagram from holographic Einstein–Maxwell–Dilaton models*, *Prog. Part. Nucl. Phys.* **135** (2024) 104093 [2307.03885].
- [119] C. Hoyos, N. Jokela and A. Vuorinen, *Holographic approach to compact stars and their binary mergers*, *Prog. Part. Nucl. Phys.* **126** (2022) 103972 [2112.08422].
- [120] M. Järvinen, *Holographic modeling of nuclear matter and neutron stars*, *Eur. Phys. J. C* **82** (2022) 282 [2110.08281].
- [121] V. Faraoni and E. Gunzig, *Einstein frame or Jordan frame?*, *Int. J. Theor. Phys.* **38** (1999) 217 [astro-ph/9910176].
- [122] Y.M. Cho, *Reinterpretation of Jordan-Brans-Dicke theory and Kaluza-Klein cosmology*, *Phys. Rev. Lett.* **68** (1992) 3133.
- [123] N. Sk and A.K. Sanyal, *Why scalar–tensor equivalent theories are not physically equivalent?*, *Int. J. Mod. Phys. D* **26** (2017) 1750162 [1609.01824].
- [124] S. Capozziello, P. Martin-Moruno and C. Rubano, *Physical non-equivalence of the Jordan and Einstein frames*, *Phys. Lett. B* **689** (2010) 117 [1003.5394].
- [125] C. Corda, *Gravitational wave astronomy: the definitive test for the 'Einstein frame versus Jordan frame' controversy*, *Astropart. Phys.* **34** (2011) 412 [1010.2086].
- [126] I. Quiros, R. Garcia-Salcedo, J.E. Madriz Aguilar and T. Matos, *The conformal transformation's controversy: what are we missing?*, *Gen. Rel. Grav.* **45** (2013) 489 [1108.5857].
- [127] A. Macías and A. García, *Jordan Frame or Einstein Frame?*, *Gen. Relativ. Gravitation* **33** (2001) 889.
- [128] M. Galaverni and G.G. S. J., *Jordan and Einstein frames from the perspective of $\omega=-3/2$ Hamiltonian Brans-Dicke theory*, *Phys. Rev. D* **105** (2022) 084008 [2110.12222].
- [129] S. Nojiri, O. Obregon, S.D. Odintsov and V.I. Tkach, *String versus einstein frame in an ads/cft induced quantum dilatonic brane-world universe*, *Phys. Rev. D* **64** (2001) 043505.
- [130] L. Jarv, P. Kuusk and M. Saal, *Scalar-tensor cosmology at the general relativity limit: Jordan versus Einstein frame*, *Phys. Rev. D* **76** (2007) 103506 [0705.4644].
- [131] S. Mahapatra and P. Roy, *On the time dependence of holographic complexity in a dynamical Einstein-dilaton model*, *JHEP* **11** (2018) 138 [1808.09917].
- [132] I. Aref'eva and K. Rannu, *Holographic Anisotropic Background with Confinement-Deconfinement Phase Transition*, *JHEP* **05** (2018) 206 [1802.05652].
- [133] I.Y. Aref'eva, K. Rannu and P. Slepov, *Holographic anisotropic model for light quarks with confinement-deconfinement phase transition*, *JHEP* **06** (2021) 090 [2009.05562].
- [134] J. Alanen, K. Kajantie and V. Suur-Uski, *A gauge/gravity duality model for gauge theory thermodynamics*, *Phys. Rev. D* **80** (2009) 126008 [0911.2114].
- [135] S. Mahapatra, S. Priyadarshinee, G.N. Reddy and B. Shukla, *Exact topological charged hairy black holes in AdS Space in D-dimensions*, *Phys. Rev. D* **102** (2020) 024042 [2004.00921].
- [136] S. Priyadarshinee, S. Mahapatra and I. Banerjee, *Analytic topological hairy dyonic black holes and thermodynamics*, *Phys. Rev. D* **104** (2021) 084023 [2108.02514].
- [137] S. Priyadarshinee and S. Mahapatra, *Analytic three-dimensional primary hair charged black holes and thermodynamics*, *Phys. Rev. D* **108** (2023) 044017 [2305.09172].
- [138] A. Daripa and S. Mahapatra, *Analytic three-dimensional primary hair charged black holes with Coulomb-like electrostatics and their thermodynamics*, *Phys. Rev. D* **109** (2024) 124039 [2401.04561].

- [139] S. He, S.-Y. Wu, Y. Yang and P.-H. Yuan, *Phase Structure in a Dynamical Soft-Wall Holographic QCD Model*, *JHEP* **04** (2013) 093 [[1301.0385](#)].
- [140] S.S. Gubser, *Curvature singularities: The Good, the bad, and the naked*, *Adv. Theor. Math. Phys.* **4** (2000) 679 [[hep-th/0002160](#)].
- [141] P. Breitenlohner and D.Z. Freedman, *Positive Energy in anti-De Sitter Backgrounds and Gauged Extended Supergravity*, *Phys. Lett. B* **115** (1982) 197.
- [142] M. Sandri, *Numerical calculation of lyapunov exponents*, *Mathematica Journal* **6** (1996) 78.
- [143] A. Wolf, J.B. Swift, H.L. Swinney and J.A. Vastano, *Determining lyapunov exponents from a time series*, *Physica D: nonlinear phenomena* **16** (1985) 285.
- [144] G.S. Bali, F. Bruckmann, G. Endrodi, Z. Fodor, S.D. Katz, S. Krieg et al., *The QCD phase diagram for external magnetic fields*, *JHEP* **02** (2012) 044 [[1111.4956](#)].
- [145] M. D’Elia, L. Maio, F. Sanfilippo and A. Stanzione, *Confining and chiral properties of QCD in extremely strong magnetic fields*, *Phys. Rev. D* **104** (2021) 114512 [[2109.07456](#)].
- [146] M.C. Gutzwiller, *Soft chaos and the kam theorem*, in *Chaos in Classical and Quantum Mechanics*, (New York, NY), pp. 116–141, Springer New York (1990), [DOI](#).